3

Synthesis and Properties of the Arrays of Magnetically Functionalized Carbon Nanotubes

Vladimir Labunov[1], Alena Prudnikava[1], Kazimir Yanushkevich[2], Aleksander Basaev[3], Alexander Danilyuk[1], Yulia Fedotova[4] and Boris Shulitskii[1]

[1]*Belarussian State University of Informatics and Radioelectronics,*
[2]*Institute of Solid-State and Semiconductor Physics NASB,*
[3]*Scientific and Manufacturing Complex "Technological Centre,"Moscow Institute of Electronic Technology,*
[4]*National Scientific and Educational Centre of Particle and High-Energy Physics BSU,*
[1,2,4]*Belarus,*
[3]*Russia*

1. Introduction

Carbon nanotubes (CNTs) are carbon molecules with a unique combination of specific mechanical, electrical, emission, optical and chemical properties. Over the last fifteen years, these objects have not ceased to amaze with regularly revealed new effects and applications (Harris, 2002).

A substantial step forward in the development of nanotechnologies is the use of carbon nanotubes filled with nanoparticles consisting of different materials. The resulting nanocomposites exhibit properties of both encapsulated and encapsulating materials with promising synergetic effects. This leads to a considerable additional contribution to the potentialities of their use in microelectronic and nanoelectronic devices (Labunov & Shulitski, 2005). One of the promising directions in this field is the investigation of the properties of carbon nanotubes combined with magnetic materials (Labunov, 2006), because there arises a possibility of synthesizing magnetically functionalized carbon nanotubes, in particular, multiwall carbon nanotubes filled with ferromagnetic nanoparticles.

Nanostructuring of a massive magnetic material substantially affects its magnetic properties. For example, the coercive force decreases, while the magnetic permittivity and the saturation magnetization increase with a decrease in the grain size to 40–20 nm. This effect is enhanced in the case of very small grain sizes (of the order of one domain). As a consequence, the magnetic vectors of atoms in an external magnetic field are identically oriented within a grain, thus eliminating losses through the domain walls and neighboring domains with different magnetization directions. Materials with grains of this size can have no hysteresis and possess superparamagnetic properties. When single-domain ferromagnetic nanoparticles are embedded in a nonmagnetic matrix, this matrix weakens the magnetic interaction between nanoparticles and, hence, decreases the magnetic field required to reorient their magnetic moments. Such nanocomposites are

characterized by a giant magnetoresistance. This has opened up new possibilities for their practical applications, for example, in sensitive elements of magnetometers and magnetic read heads.

Therefore, considerable progress can be made, for example, in increasing the capacity of magnetic read– write devices owing to the use of magnetically functionalized carbon nanotubes prepared by filling of carbon nanotubes with ferromagnetic nanoparticles. In this case, the particle size can be small enough to represent a single domain and the carbon nanotube walls serve as nonmagnetic separating regions between nanoparticles.

The purpose of present review is to summarize actual results regarding synthesis of multiwall carbon nanotubes, particularly, magnetically functionalized multiwall carbon nanotubes (MFCNT), with the use of iron nanoparticles as growth catalyst and complex analysis of their crystal structure, composition, and magnetic properties as a function of peculiarities of synthesis procedure.

2. Preparation of carbon nanotubes

Generally, there are several techniques for introducing a material into carbon nanotube cavities (Harris, 2002). One of the techniques is conventional evaporation of carbon in an arc discharge with the use of an anode containing the material that should be encapsulated. For the most part, this technique is applicable to materials that can "survive" under extreme conditions of electric arc discharge. The second technique consists in chemically opening the ends of closed nanotubes, followed by introducing a filler compound inside nanotubes due to the capillary effect. This method proved to be better than the first technique and can be used for incorporating fillers from melts (liquid phases) and even in the case of biological molecules. The third technique involves the synthesis of carbon nanotubes through the high-temperature pyrolysis of liquid hydrocarbons in a mixture with a volatile catalyst, providing the growth of carbon nanotubes. Catalyst nanoparticles, deposited on a substrate, initiate the growth of carbon nanotubes. Moreover, during growth they are embedded in carbon nanotubes over their entire length and even occupy the ends of the nanotubes. Consequently, this technique is most appropriate for obtaining MFCNT. It is this technique that was used in our work for preparing multiwall carbon nanotubes filled with particles of iron, which is the most widely used magnetic compound among the triad of iron, cobalt, and nickel. Carbon nanotubes were synthesized by high-temperature pyrolysis of liquid hydrocarbon *p*-xylene C_8H_{10} in a mixture with volatile ferrocene $[Fe(C_2H_5)_2]$ as a catalyst at atmospheric pressure with the use of argon as a gas carrier on the surface of silicon substrates [KDB 20 (100)] in a tubular quartz reactor specially designed for these purposes (Labunov, 2005). The samples for investigations were prepared under conditions of predominant growth of carbon nanotubes on the Si substrates with thermal oxide SiO_2 (0.6 μm) (Labunov et al., 2006). Ferrocene concentration c_x in p-xylene equaled 0,5, 5 and 10 %, the mixture injection rate into the reactor zone was 1 ml/min, the temperature was 775-875 °C, the argon flow rate was 100 cm^3/min, and the reaction time varied in the range 1-5 min. Under these synthesis conditions, carbon nanotube arrays were formed either on the silicon substrates or reactor walls.

3. Morphology, structure and composition of magnetically functionalized carbon nanotubes synthesized by injection CVD method

3.1 Variety of CNTs morphologies studied with transmission electron microscopy

Transmission microscopy study of CNTs synthesized by injection CVD technique revealed variety of morphologies of multiwalled CNTs, filled with particles of different Fe phases.

Fig. 1 shows typical images demonstrating formation of nanocomposites at the ends of CNTs. One should classify four main variants of metallic filler inside CNTs: at the very end of closed CNT (1), at some distance from closed end (2), nanocomposite emerges from opened CNT (3) and CNT with opened and unfilled ends (4). As evidenced from Fig. 1 all CNTs are multiwalled with diameter of 10-20 nm and should be classified as thin-walled CNTs because diameter is larger then the wall thickness. The majority of filler phase has a spherical form with the aspect ratio (length to diameter) ~5:1 - 8:1.

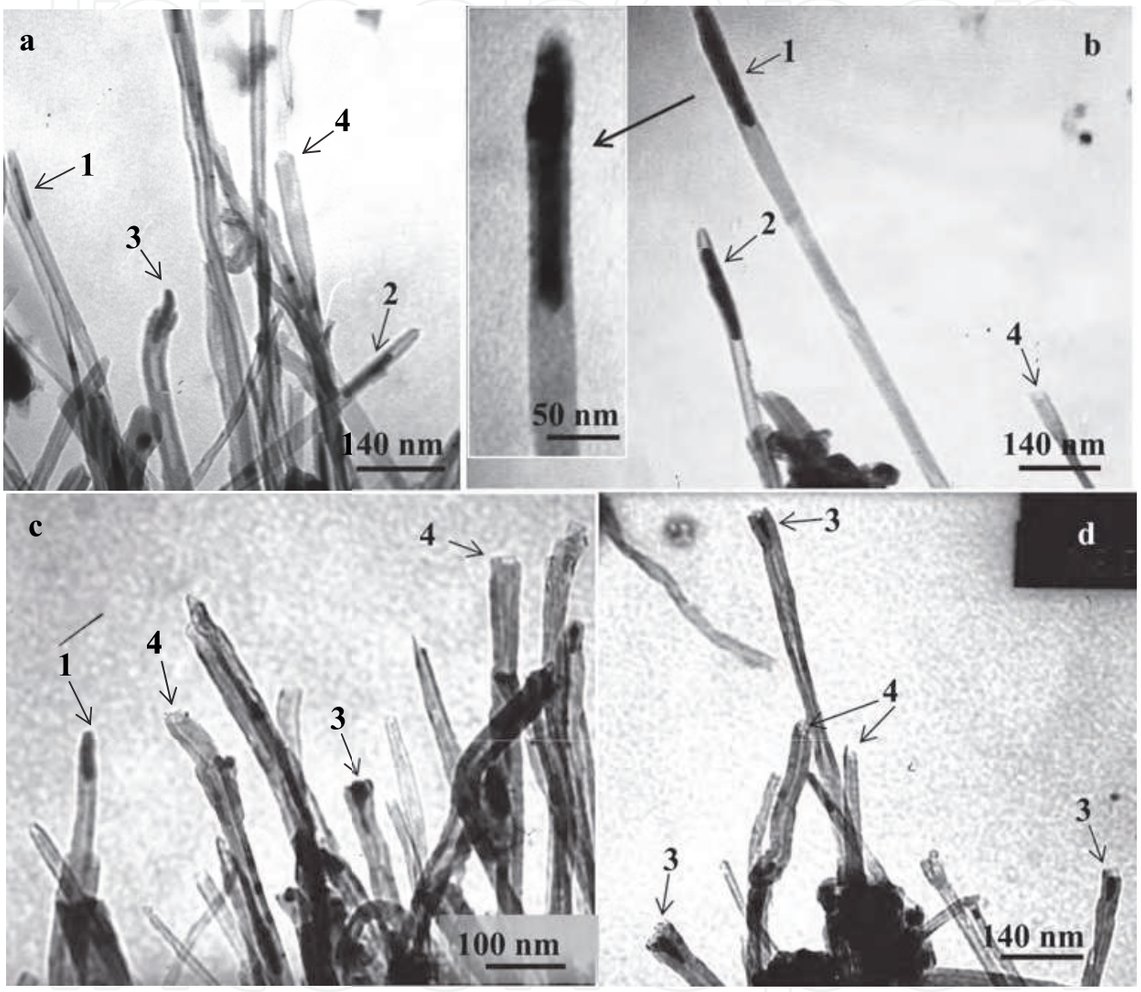

Fig. 1. TEM images of CNTs with the various geometries types of nanocomposites formed on the CNTs ends: at the very end of closed CNT (1), at some distance from closed end (2), nanocomposite emerges from opened CNT (3) and CNT with opened and unfilled ends (4).

The most typical CNT arrays morphology is presented in Fig. 2.
Microscopic image usually reveal multiwall CNTs of different shape and morphology: with unfilled channel (1), with channel filled with composite of prolonged spherical form (2); with particles of spherical form composite separated with internal walls in channel (3). Diameter of these CNTs ranged within 20-30 nm at channel diameter of 7-10 nm, i.e. they should be classified as thin-walled CNTs. Diameter of precipitations, particularly of spherical form (2), is higher so that they "swell" the channel.

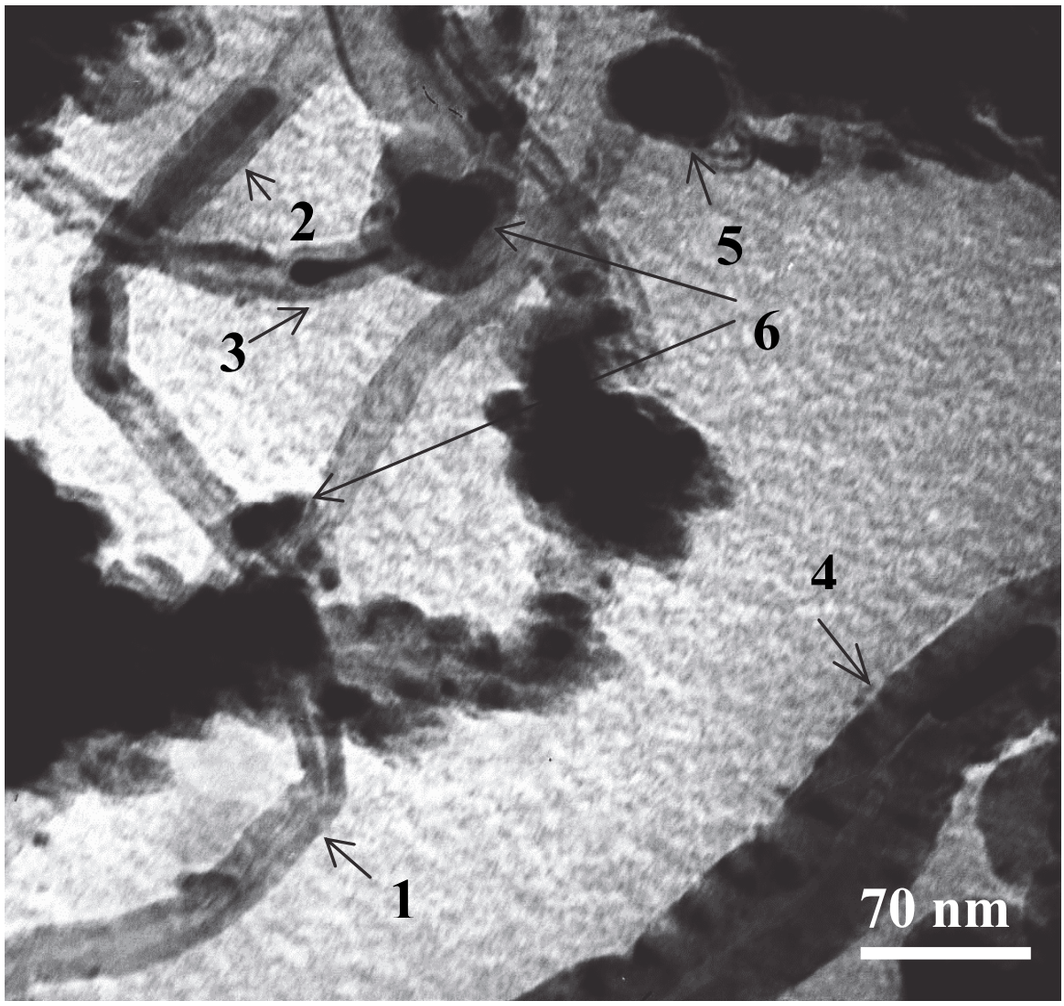

Fig. 2. The most typical morphology of multiwall CNT arrays: thin-walled - (1) with unfilled channel; (2) with channel filled with composite of prolonged spherical form; (3) with particles of spherical form composite separated with internal walls in channel; (4) thick-walled; (5) capsules; (6) obcordate form.

One should particularly consider multiwall CNTs (4) of large diameter (50-70 nm) with narrow channel (7-10 nm). Such CNTs should be classified as thick-walled. The peculiar feature of these nanotubes is that they possess nanocomposite inclusions not only inside the channel but also inside the walls (dark inclusions perpendicular to the films). Precipitation of nanocomposite filler inside walls of CNTs most probably resulted in the increase of their thickness. In so doing, multiwall CNTs should be divided into thin-walled and thick-walled CNTs. One more class of nanocomposite filler is particles incapsulated inside carbon shell (5). Unique obcordate form of nanocomposie is precipitated on the junction of two nanotubes (6). Obviously, such capsules are incorporated into the CNTs edges. Furthermore, such capsules evidence the tip-growth mechanism of CNts growth (Li, 2000).
Variants of above mentioned structures and morphology of CNTs are shown in details in Fig. 3. Different examples of CNTs, filled with nanocomposite particles with high aspect ratio, have been shown. Such particular form of inclusions support anisotropy of CNTs

magnetic properties in parallel and perpendicular directions and could be applied in magnetic recording media (Pull, 2005). Fig.3a shows thin-walled CNT with filler of variable thickness, which length equals approximately 2/3 of CNT length (1). Thick-walled «compound» CNT (2), containing areas of different thickness: channel and walls of one of them is filled with nanoparticles, the second part is thinner with empty channel, and third part –approximately up to 2/3 filled with composite. The inset in Fig.3a presents CNT with channel completely filled with composite. Combination of thin-walled CNT with channel almost completely filled with composite and capsule «fixed» on its edge is shown in Fig. 3b. Fig. 3c clearly revealed obcordate structure of CNT within the junction of two thick-walled CNTs. Channel of one of the nanotubes is filled with composite while second is empty. Simultaneously, walls of both CNts contain nanocomposite. Fig. 3b clarifies the origin of obcordate structure of CNT – it is formed due to the merging of two capsules from different structures.

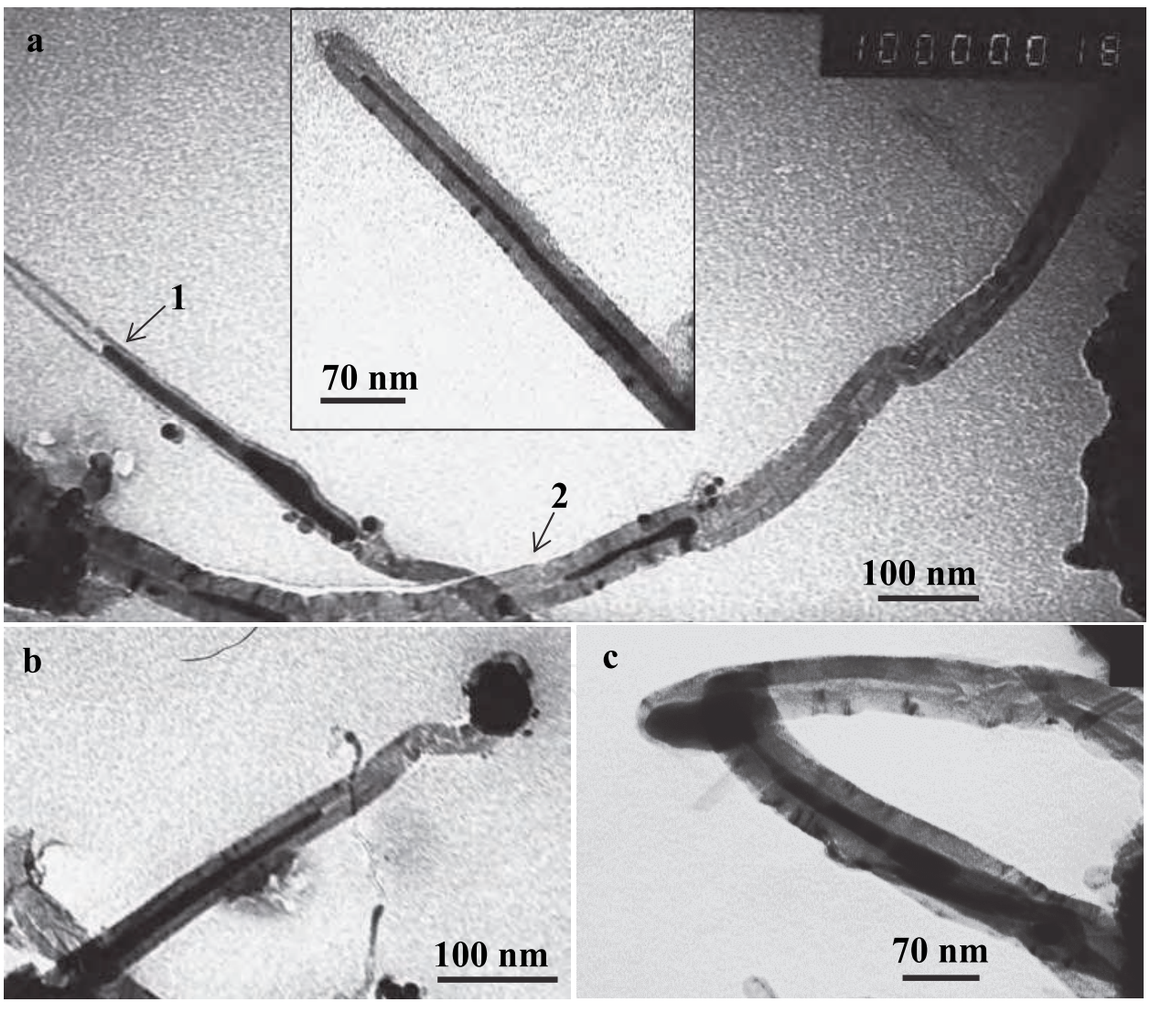

Fig. 3. Details of CNTs morphologies shown in Fig.2, with strong filling of channels: (a) separate CNTs; (b) combination of thin-walled CNTs and capsule; (c) obcordate–like form within the junction of two thick-walled CNTs.

Variety of structures and geometries of CNTs are not limited with incorporation of filler inside channel or wall of nanotubes or carbon capsules. Filler could also be located outside of the tubes – on their walls both thin- and thick-walled. Fig. 4 shows micrographs of thin-walled CNTs with nanocomposite formed outside of their walls.

As evidenced from Fig. 4, nanocomposite is located in the form of balls on the outer side of walls in CNTs. When particles are of relatively large size (20-30 nm) it is clearly seen that they are incapsulated inside the shell constituting short nanotubes, formed on the surface of the basic CNT (2). When size of particles is small (3-5 nm) just dark spots are seen (1). Possible, these particles are incapsulated as well, but in this case carbon shells cannot be clearly observed in transmission microscopy image due to their very small thickness.

Fig. 5 presents micrographs of thick-walled CNTs of different kinds: Fig. 5a – separate nanotube, Fig. 5b – combination of CNT and capsule, «fixed» on its edge (such a combination seem to be quite usual). As evidenced from Figs. 5 a and b, nanocomposite filler is located inside nanotubes and capsules (1), inside the walls (2) and on the surface of walls (3), where nanotubes are seen as incapsulated balls. Fig. 7a shows that, similarly to the case of thin-walled CNTs, balls of filler inside short nanotube is formed on the surface of basic nanotube (3). It is quite possible that all composite nanoparticles are incorporate on the nanotubes surface in such a way. However, many of them located in unfavorable configuration against electron beam in microscope so, that their ideal configuration could not be recognized. On the other hand, the majority of nanocomposite particles, located on the walls surfaces, possess disordered form (4).

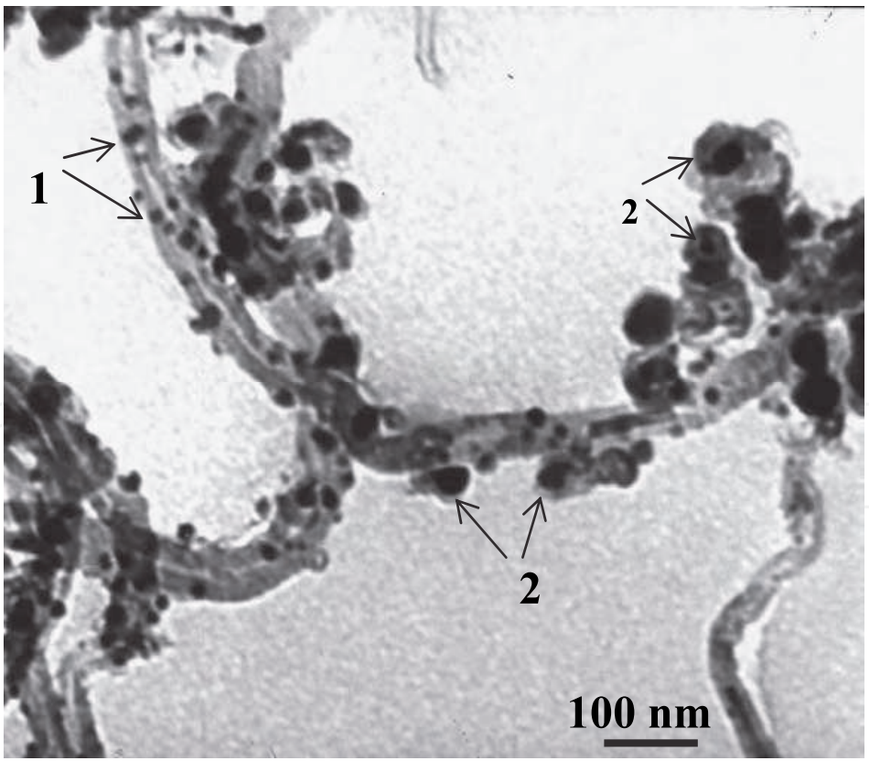

Fig. 4. Thin-walled CNTs with nanocomposite formed on the outside parts of their walls: (1) dark balls of small size (3-5 nm); (2) balls of relatively large size (20-30 nm) inside the shell of short nanotubes.

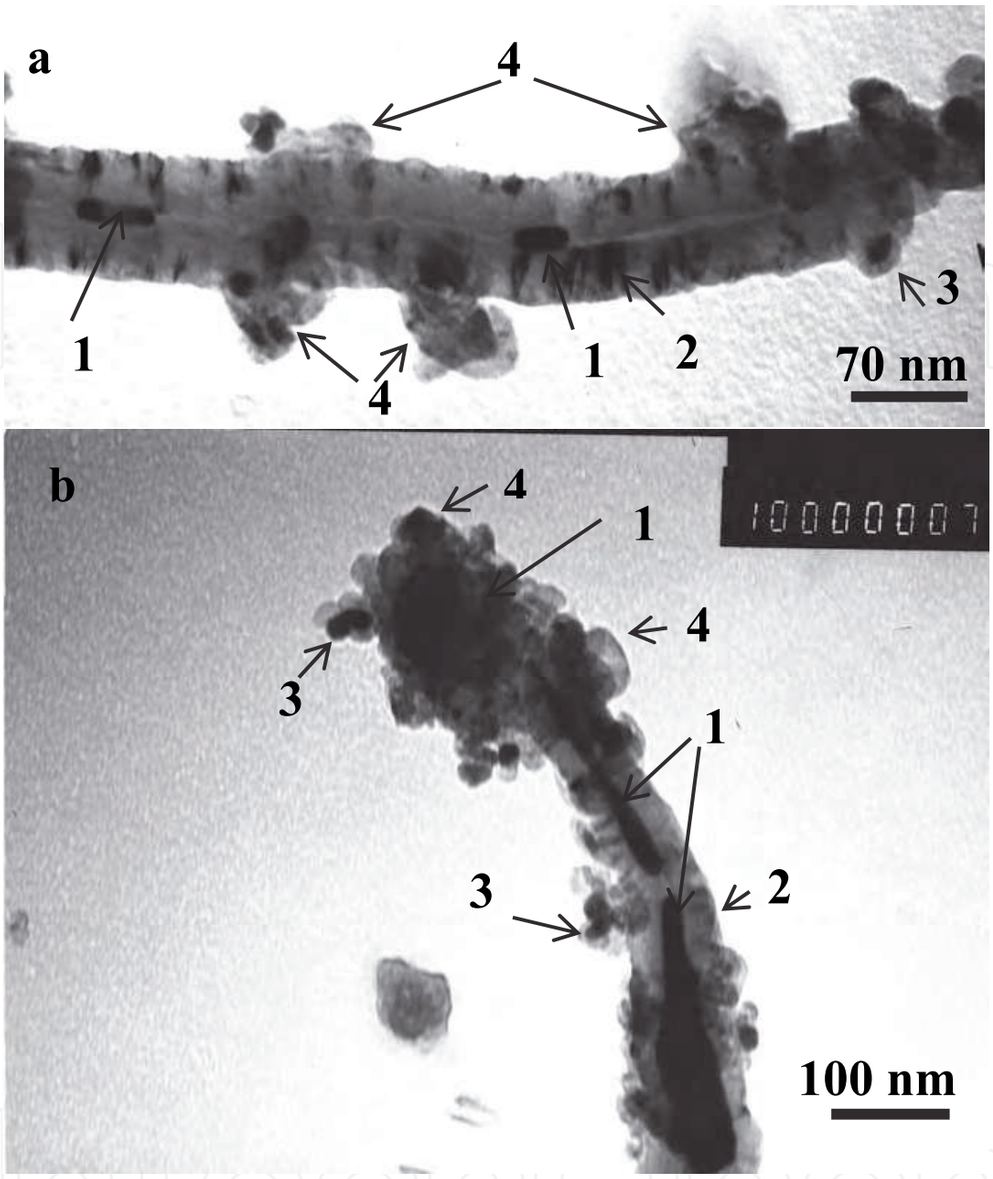

Fig. 5. Thick-walled CNTs - (a) separate nanotube; (b) combination of nanotube and capsule. Nanocomposite is located: (1) – inside the channel, (2) – inside the walls, (3) – on the surface of walls in the from of balls incapsulated inside short nanotubes, and (4) – in disordered form.

3.2 Effects of synthesis on Si substrate and on the walls of a quartz reactor

Comparative study of the morphology and composition of carbon nanotubes synthesized on Si substrate and on the walls of a quartz reactor has been performed on samples containing c_x = 10 %. The external appearance of the carbon nanotube arrays is shown in Fig. 6. It can be seen from Fig. 6 that the array of vertically aligned close-packed carbon nanotubes is formed under the abovementioned synthesis conditions. Bright inclusions against the dark background of the array cleavage wall (Fig. 6a) and the array surface are characteristics of the image. The carbon nanotubes located at the center of the array cleavage wall are shown

in Fig. 6b. It can be seen that the carbon nanotubes are broken and bent. The bending of the carbon nanotubes can suggest that, in the array, there are internal stresses, which lead to deformation of nanotubes after cleavage. Bright inclusions are clearly seen at the ends of broken carbon nanotubes. This indicates the presence of metal-containing particles. Rather long bright arc regions in the image of the nanotube array can result from illumination upon focusing of the electron beam of the microscope. Since metal-containing segments of nanotubes are observed at the center of the height of the array, we can assume that they are also located inside the carbon nanotubes along their entire length. As can be seen from Fig. 6c, disordered nanostructures of different configurations are formed at the array surface. This phenomenon is typical of the synthesis for carbon nanotubes through the high-temperature pyrolysis of liquid hydrocarbons in a mixture with a volatile catalyst. At the instant of completion of pyrolysis synthesis, the synthesis conditions change abruptly, deviate from optimum, and prevent orientated growth of carbon nanotubes. The presence of bright regions in the image of the array surface also indicates that metal-containing nanoparticles are contained at the surface.

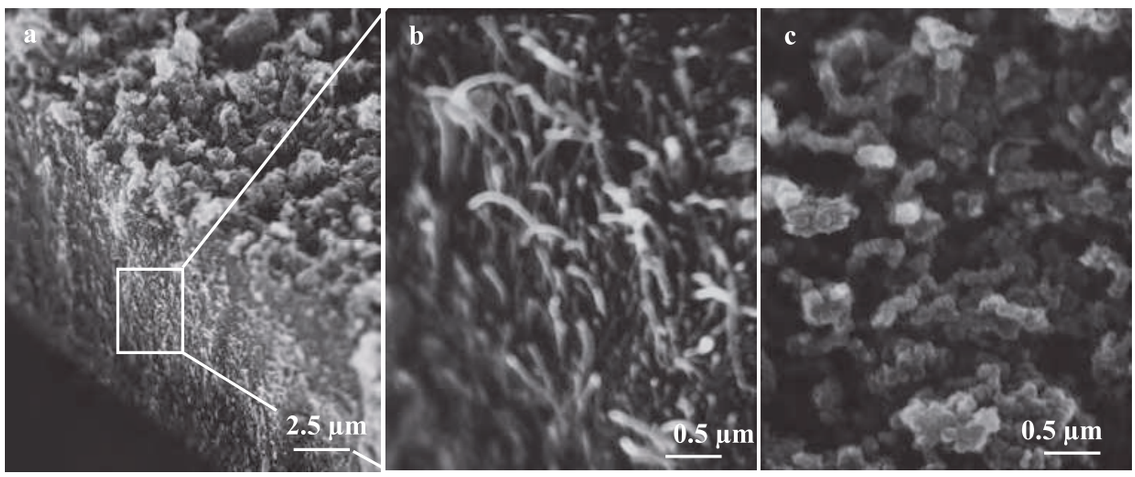

Fig. 6. Images of carbon nanotubes synthesized on Si substrate and on the walls of a quartz reactor: (a) axonometric view of carbon nanotube arrays (vertical wall of array cleavage and array surface), low magnification; (b) vertical wall of array; and (c) carbon nanotube array surface, high magnification.

To identify phase composition of carbon nanotubes synthesized on the Si substrates and formed at the walls of the quartz reactor XRD analysis was performed at room temperature. The X-ray diffraction data (Cu *K* radiation) were collected by point sampling with an angle step of $\Delta 2\theta = 0.03°$. The exposure time per each angle point was $\Delta\tau = 5$ s. The X-ray diffraction patterns of the carbon nanotubes of both types are depicted in Fig. 7. For the carbon nanotubes synthesized on the silicon substrate, the X-ray diffraction pattern (Fig. 7a) in the angle range $5^\circ \le 2\theta \le 30^\circ$ contains a set of low-intensity reflections that can be assigned to amorphous carbon in the composition of the soot and graphite.

The X-ray diffraction pattern in the angle range $5^\circ \le 2\theta \le 80^\circ$ involves high-intensity reflection (400) from the Si substrate a series of low-intensity reflections that can be used for determining the composition of the composite under investigation. Somewhat unexpectedly, the identification of the X-ray diffraction patterns revealed that Fe_3C cementite is the main component of carbon nanotubes. The reflections indexed as (112), (201), (211), (122), (004),

(222), and (313) for Fe_3C cementite (Lipson & Steeple, 1970) are clearly seen in the X-ray diffraction pattern. Iron in the form of the (110) and (200) reflections and the Fe_5C_2 carbide in the form of the (021) (Lipson & Steeple, 1970) reflection manifest themselves in the X-ray diffraction pattern. The carbon nanotubes deposited on the reactor walls were mechanically separated from the walls in the form of a powdered material. The X-ray powder diffraction pattern of the carbon nanotube powder (Fig. 7b) contains a halo of amorphized carbon at small angles 2θ and a pronounced (111) reflection of graphite with a rhombohedral structure (ICDD card no. 75-2078, PCPDFWIN) (JCPDS, 1998). This structure is characteristic of carbon nanotubes. At larger angles, the X-ray powder diffraction pattern exhibits a series of lines corresponding to the Fe_3C, Fe, and Fe_5C_2 phases, the intensities of which are considerably higher than those of lines shown in Fig. 7a. Analysis of the X-ray powder diffraction pattern in Fig. 2b also demonstrates that the Fe_3C cementite with an orthorhombic structure (space group Pbnm) dominates over the other components in the sample under investigation. A comparison between the areas of the reflections (with allowance made for the overlapping reflections) shows that the Fe_3C content in the composite with respect to the Fe and Fe_5C_2 contents is more than 90 %. By using the techniques for identifying the orthorhombic structure and its quadratic form (Lipson & Steeple, 1970)

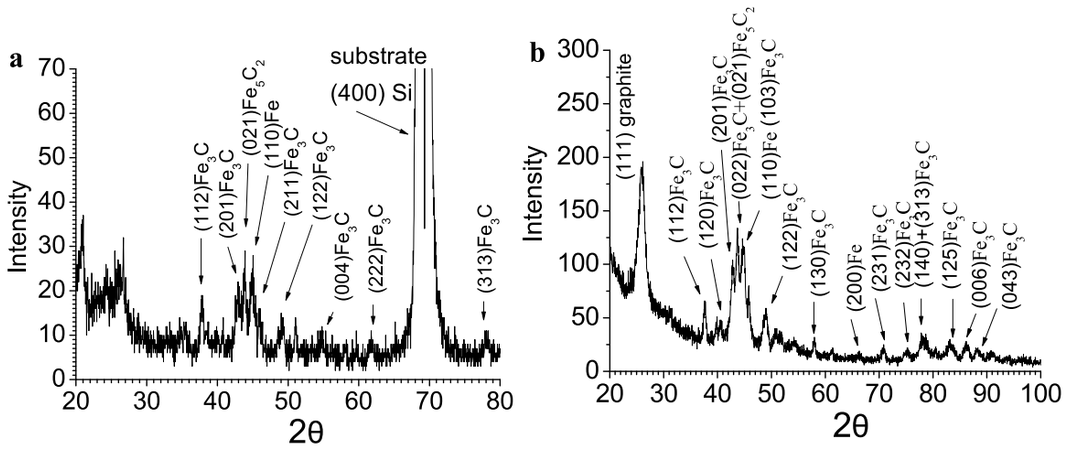

Fig. 7. XRD patterns of carbon nanotubes: (a) synthesized on Si substrates and (b) on quartz reactor walls.

$$\sin^2\theta_{\lambda kl}=\frac{\lambda^2}{4a^2}h^2+\frac{\lambda^2}{4b^2}k^2+\frac{\lambda^2}{4c^2}l^2 \quad (1)$$

the unit cell parameters of the Fe_3C phase in the carbon nanotubes were determined. It should be noted that the numbers of the reflections corresponding to the Fe_3C phase in the X-ray diffraction patterns in Figs. 7a and 7b are sufficient for this purpose. The calculated unit cell parameters are as follows: a=0.452 nm, b=0.508 nm, and c=0.672 nm. This is in good agreement with the corresponding unit cell parameters a = 4.518 Å, b = 5.069 Å, and c = 6.736 Å available in the ICDD database (card nos. 76-1877 and 75-0910, PCPDFWIN) (JCPDS, 1998) for the polycrystalline compound Fe_3C.

The results are undeniably of theoretical and practical interest. The dominance of the Fe_3C cementite in the composition of the carbon nanotubes indicates that, during their growth, Fe catalyst particles are not only embedded in the carbon nanotube, they also interact with the

nanotube with the formation of the stable compound Fe_3C, which in the massive polycrystalline form possesses pronounced ferromagnetic properties. From the practical viewpoint, this will make it possible to use magnetically functionalized carbon nanotubes for fabricating reliable microelectronic and nanoelectronic devices resistant to external actions.

Further investigation of carbon nanotubes has been performed by transmission electron microscopy. For this purpose, the carbon nanotubes were dispersed on a carbon microgrid of a high-resolution electron microscope. The experimental results are presented in Fig. 8.

It is known that electron diffraction patterns of carbon nanotubes, especially when they are obtained for multiwall nanotubes, are difficult to interpret (Pull, 2005). However, qualitative analysis of the electron diffraction patterns of the samples under investigation (Fig. 8a) demonstrates a good correlation with the X-ray diffraction data. The halo associated with the amorphized carbon is rather pronounced. The electron diffraction pattern contains (002) and (004) reflections of the graphite. Possibly, these reflections overlap with the (002) and (004) reflections of the cementite (PDF no. 76-1877). This is the most real situation, because, according to the contrast, all inclusions in nanotubes are nanocrystals and, hence, should also be characterized by point reflections. Moreover, it is clear that a coherent interface $(002)_{graphite}$ II $(002)_{Fe3C}$ should occur between the graphite and the carbide. As regards ring reflections, they can be associated with the graphite. Furthermore, the weak reflections (110) and (211) attributed to the iron particles are observed in the electron diffraction pattern. The image of the array of misoriented carbon nanotubes is displayed in Fig. 8b. It can be seen from this figure that a large number of black dots and horizontally located nanotubes occur in the image. The black dots can correspond either to filler particles at the ends of the nanotubes located perpendicular to the substrate or to magnetic nanoparticles encapsulated by carbon. It is evident that filler nanoparticles are characterized by a considerable size dispersion. It should be noted that the size of encapsulated particles exceeds their size in nanotubes and is in the range ~40–50 nm. The diameter of the nanotubes located in the horizontal plane varies from ~5 to ~40 nm. The original images in which it is possible to see both nanotubes and nanocapsules are displayed in Figs. 8c and 8d. It can be seen from these figures that the nanotubes are multiwall and their outside diameter varies from ~20 to ~40 nm. The diameter of filler nanoparticles is smaller and ranges from ~5 to ~20 nm. The two nanotubes and a dumbbell-like nanocapsule are clearly seen in Fig. 8c. One of the nanotubes has an empty channel, and the other nanotube is filled with oval nanoparticles (~5–20 nm in diameter) separated by walls. A carbon nanotube array fragment also involving two nanotubes and a nanocapsule is shown in Fig. 8d. In this case, too, one nanotube has an empty channel and the neighboring nanotube contains elongated nanoparticles ~5 nm in diameter and ~80 nm in length.

Therefore, investigations of carbon nanotubes by transmission electron microscopy permitted us to determine the ranges of the nanotube and filler particle sizes. It was established that filler inclusions in the carbon nanotubes have different configurations and different sizes and are differently embedded in the nanotubes. Analysis of the electron microscope images demonstrated that the outside diameters of multiwall carbon nanotubes and filler particles (located inside nanotubes) are characterized by large size dispersion. Moreover, it was revealed that the samples contain an insignificant number of single-wall carbon nanotubes.

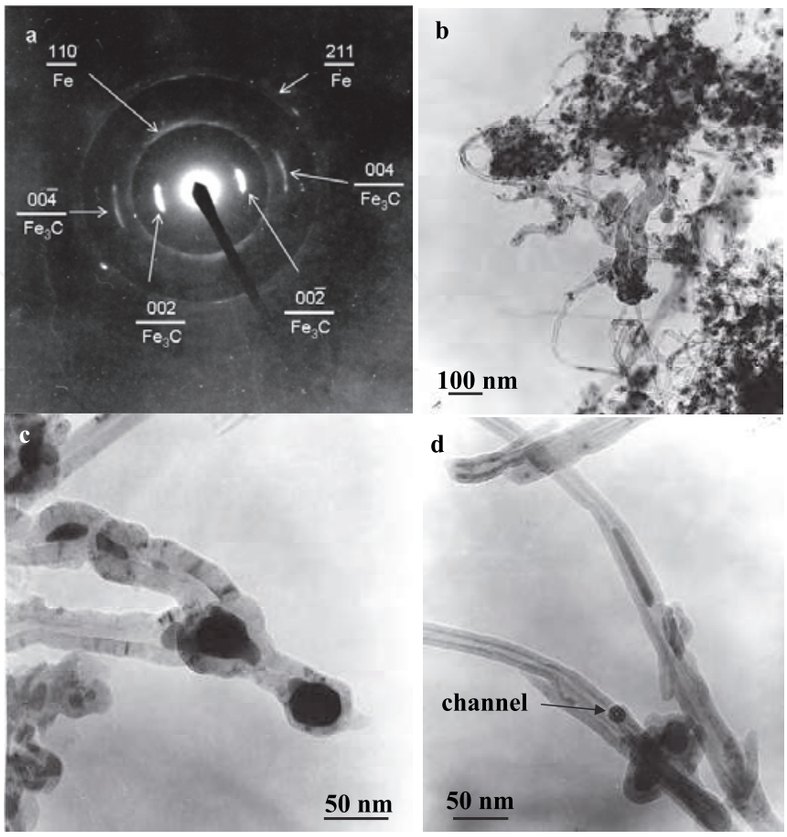

Fig. 8. Electron microscopic data: (a) electron diffraction pattern, (b) general view of disordered carbon nanotube array, and (c, d) fragments of two nanotubes and a nanocapsule.

3.3 Effects of catalyst concentrations during injection CVD synthesis

Typical TEM images of CNTs synthesized at various concentrations of ferrocene c_x in the feeding solution are presented in fig.9: (a) 0.5 %; (b, c) 5 %; (d) 10 %. It is seen, that CNTs are multi-wall. Their outer diameters vary from ~20 to ~80 nm. The diameters of the nanoparticles inside CNTs are smaller and reach ~30 nm. It is worthy to note that all the CNT arrays synthesized by us (with 0.5 %, 5 %, and 10 % of ferrocene) are composed of nanotubes with the inclusions of all the types represented in Fig. 9 (a-d), but the inclusion shapes shown in Fig. 9 (a) are more typical for 0.5 %-samples, in Fig. 9 (b) - for 5 %-samples and in Fig. 9 (c, d) - for 10 %-samples.

The XRD data (Cu$K\alpha$ radiation) performed at room temperature were collected by point sampling with an angle step of $\Delta 2\theta$=0.03°. The exposure time per each angle point was $\Delta\tau$=5 s. The XRD patterns of the CNTs of three types are depicted in Fig. 10 (a, b, c). All the XRD patterns contain a halo of amorphous carbon at small angles 2θ and a pronounced (111) reflection of graphite with a rhombohedral structure (ICDD card no. 75-2078, PCPDFWIN) (JCPDS, 1998). This structure is characteristic of carbon nanotubes. At larger angles, the X-ray powder diffraction pattern exhibits a series of lines corresponding to the F_3C, α-Fe and Fe_5C_2 phases. Analysis of the X-ray powder diffraction data demonstrates that the F_3C cementite with an orthorhombic structure (space group Pbnm) dominates over the other

components in the samples under investigation. A comparison between the areas of the reflections (with allowance made for the overlapping reflections) shows that the F_3C content in the composite with respect to the α-Fe and Fe_5C_2 contents is more than 90%. The calculated in our previous work unit cell parameters are as follows: a = 0.452 nm, b = 0.508 nm and c = 0.672 nm (Basaev, 2008).

Comparing figures 10 a, b and c one can conclude that the higher is the catalyst concentration in the feeding solution, the higher will be the content of Fe_3C and α-Fe phases in the MFCNTs filler. The XRD pattern corresponding to 10 %-specimen contains not only the most intense reflex (110) of α-Fe at $2\theta \approx 44.7^{o}$, but also a sufficiently remote the second by the intensity reflex of pristine Fe (211) at $2\theta \approx 82.4^{o}$. As the concentration c_x increases, the intensity of the carbide phase reflexes also increases not only at small angles, but also at sufficiently large angles 2θ.

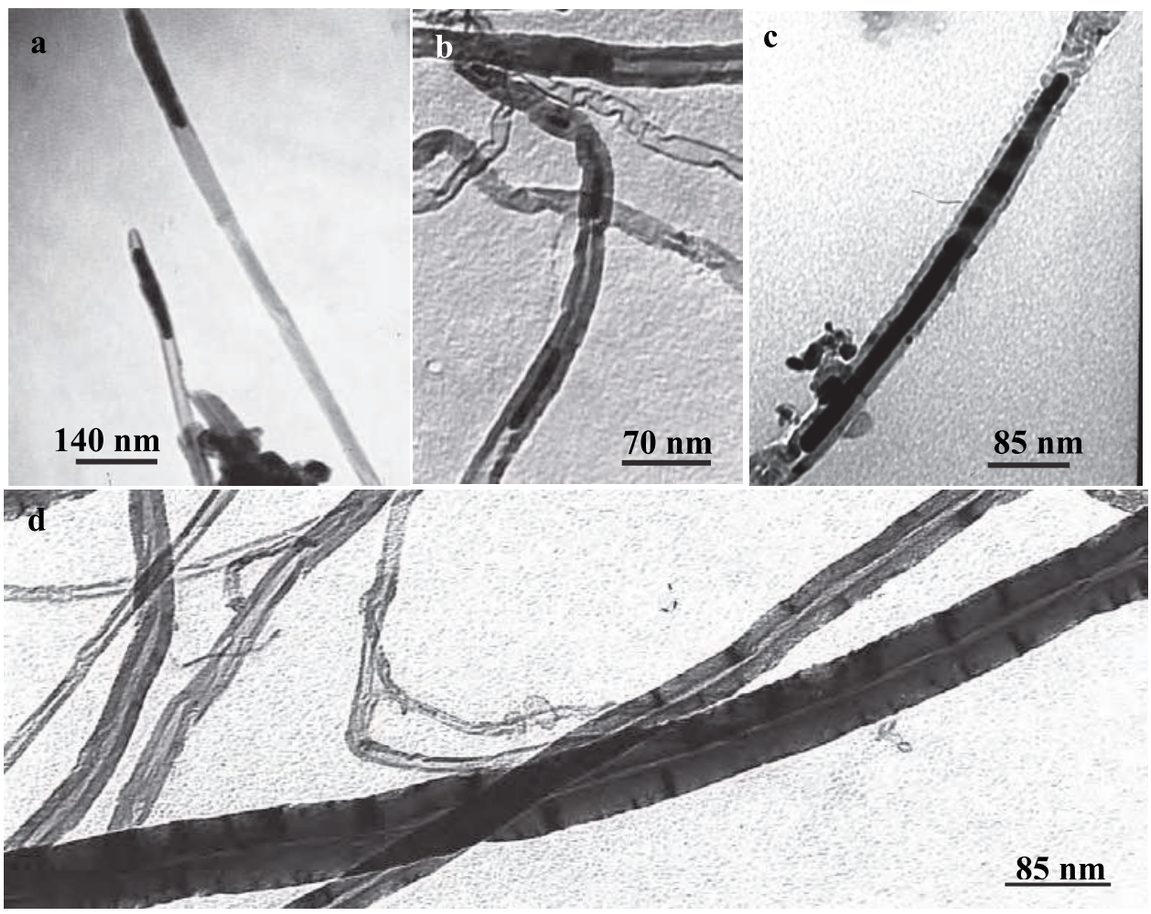

Fig. 9. Typical TEM images of CNTs synthesized at various concentrations of ferrocene in the feeding solution: (a) 0.5 %; (b) 5 %; (c, d) 10 %.

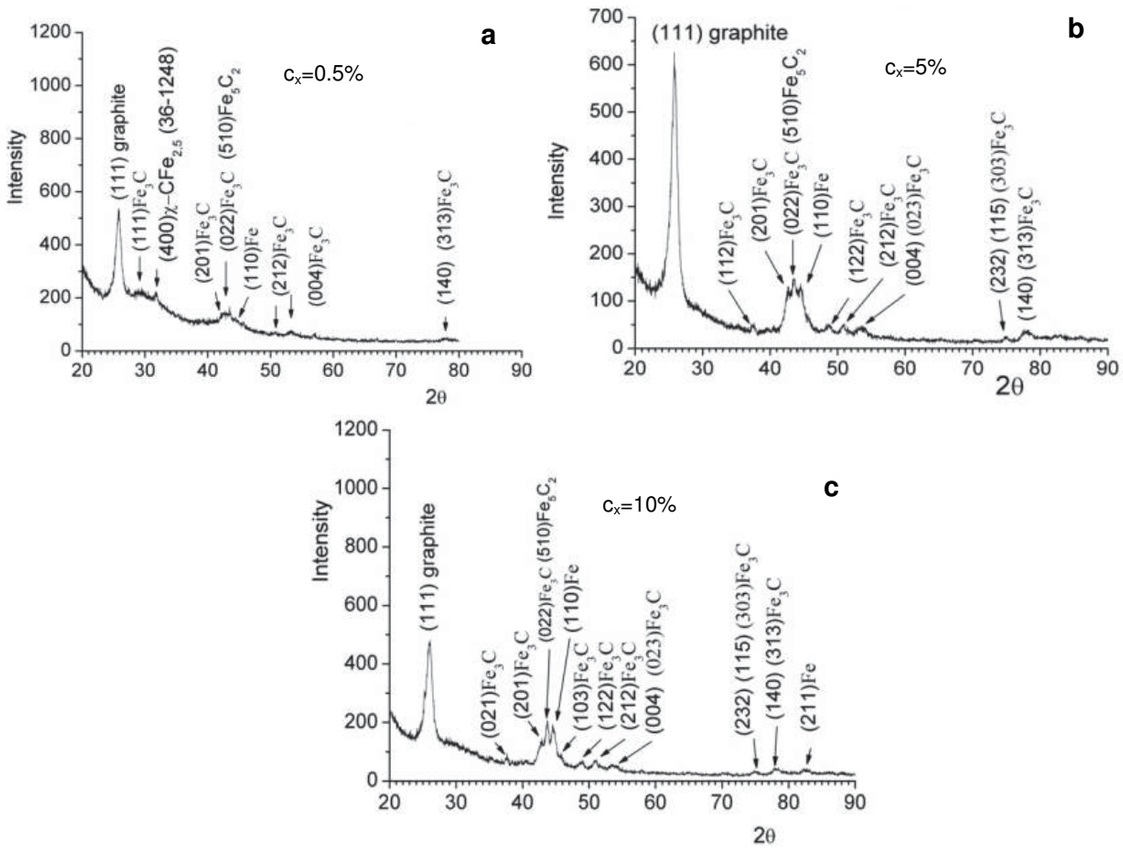

Fig. 10. XRD patterns of the powdered CNTs synthesized at various concentrations c_x of ferrocene in the feeding solution: (a) 0.5 %, (b) 5 %, and (c) 10 %.

4. Magnetic properties of CNT arrays synthesized by the injection CVD method at various catalyst concentrations

The specific magnetization of the synthesized MFCNTs was measured by the static ponderomotive method (Chechernikov, 1969). The dependences $\sigma(T)$ were obtained in the temperature range 78 K ≤ T < 600 K in the magnetic field H = 0.86 T (the magnetic field gradient across a sample region $\Delta Z \approx$ 3.0 cm was $dH_Z/dx \approx$ 0.16 T cm^{-1}). The temperature dependences $\sigma(T)$ were measured upon heating of the samples from liquid-nitrogen temperature. The temperature dependence $\sigma(T)$ upon heating in the temperature range 78 K≤T<1100 K that clearly reflects a sequence of manifestations of all magnetic phases of the filler in CNTs and a variation in their specific magnetization with an increase in the temperature was demonstrated by us in (Basaev et al., 2008).

The dependences σ (T) for the nanotube powders under investigation are plotted in Fig. 11 (a-c). The anomalous point in the dependence $\sigma(T)$ corresponds to the Curie point T_C ~ 480 K for cementite Fe_3C (Chikazumi, 1980).

According to this data, the increase of ferrocene content in the feeding solution leads to the increase of the specific magnetization of the CNT array both at liquid-nitrogen temperature and in the whole temperature range while the magnetic order of Fe_3C exists (up to its Curie

point, T_C ~480 K). Noteworthy, the specific magnetization increases also at the temperatures higher T_C for Fe_3C: from ~0.6 A m²/kg for c_x= 0.5 % to ~4.5 A m²/kg for c_x= 10 %. This phenomenon could be only explained by the presence of bigger amount of the magnetic filler inside the nanotubes formed at higher catalyst concentrations. Noticeably, the character of $\sigma(T)$ curve for 0.5 % differs from 5 % and 10 %: it has an almost horizontal plateau up to 300 K, but the curves corresponding to the other two samples do not.

We conducted some theoretical investigations and estimated that the obtained experimental dependence of the specific magnetization of the sample with c_x=10 % in the temperature range of 80-300 K satisfies Bloch law:

$$M(T) = M(0)[1 - BT^{3/2} - CT^{5/2}], \quad (2)$$

and at temperatures 300-480 K it corresponds to Stoner law:

$$M(T) = M(0)[1 - (T / T_C)^2]^{1/2}, \quad (3)$$

where $M(0)$ is saturation magnetization at zero temperature, T_C is Curie temperature of Fe_3C, B=1.65·10^{-5} K$^{-3/2}$, C~10^{-8} K$^{-5/2}$.

The temperature dependence of magnetization of the sample with c_x=5% also correspond to Bloch law, but in the temperature range of 80-450 K. Here the Bloch constant B=6.1·10^{-5} K$^{-3/2}$. Taking into account that the magnetization of 10 %-sample is three times the magnetization of 5 %-sample (Fig. 12-13), the exchange constant which characterizes the exchange interaction in case of c_x=10% is less than when c_x=5%. The observed weakening of the exchange interaction is natural property of the films consisting of ultra thin magnetic layers, and can relate both to dimensional effect and the consequence of decreasing of the effective magnetic momentum of Fe atoms. The thickness of the interface where CNT change the electronic structure of Fe varies from 1 nm to 2-5 nm. The essential changes in the $\sigma(T)$ dependence occur when the thickness of magnetic inclusions is smaller than the doubled thickness of the interface, i.e. when the interfaces of the inclusions overlap (Komogortsev et al., 2007).

The Fe inclusions as their sizes decrease can retain their magnetic properties up to thicknesses of 2-3 nm. Their magnetic properties can degrade significantly at large sizes, when, for example, they contact the interlayer material, so the average atomic magnetic moment decreases and the exchange interaction become weaker. This effect spreads into the depth of 2-5 nm and, probably, can be related to the interlayer stirring which leads to changes in the electronic structure of Fe localized on the surface interfaces (Varnakov et al., 2007).

The hysteresis loops of the samples, obtained at 0.5 % of ferrocene in the feeding solution (c_x = 0.5 %) at low temperatures (10 K) showed diamagnetic nature of the material what might be caused by the insufficient sensitivity of the equipment. Taken at different temperatures, the hysteresis loops of non oriented blocks of MFCNT arrays synthesized at c_x = 5 % and c_x = 10 % are presented in Fig. 12 and Fig. 13, correspondingly. All the curves are symmetrical. In 5 %-sample (Fig. 5) the hysteresis loop area decreases with increasing the temperature.

In 10 %-sample (Fig. 13), on the contrary, as the temperature increases the hysteresis loop area slightly increases. As a result, with increasing the temperature the taken from the loops coercivity H_c decreases for the sample with c_x = 5 %, but slightly increases (for ~35 mT=0.35 kOe at 287 K comparing with 10 K) for 10%-sample. The residual magnetization M_r and the

saturation magnetization M_s decrease with increasing the temperature for both samples. At that, the M_r and M_s values of 10%-sample are higher than that of 5%-sample in the whole temperature range. In particular, the difference ΔM_r reaches ~0.1 emu/g at 10 K, ~0.09 emu/g at 287 K, and the difference ΔM_s ~0.22 emu/g at 10 K, ~0.20 emu/g at 287 K. However, coercivity $H_c(c_x$=10%) smaller than $H_c(c_x$=5 %), especially at low temperatures when difference between them reaches ~0.73 kOe (0.073 T) at 10 K.

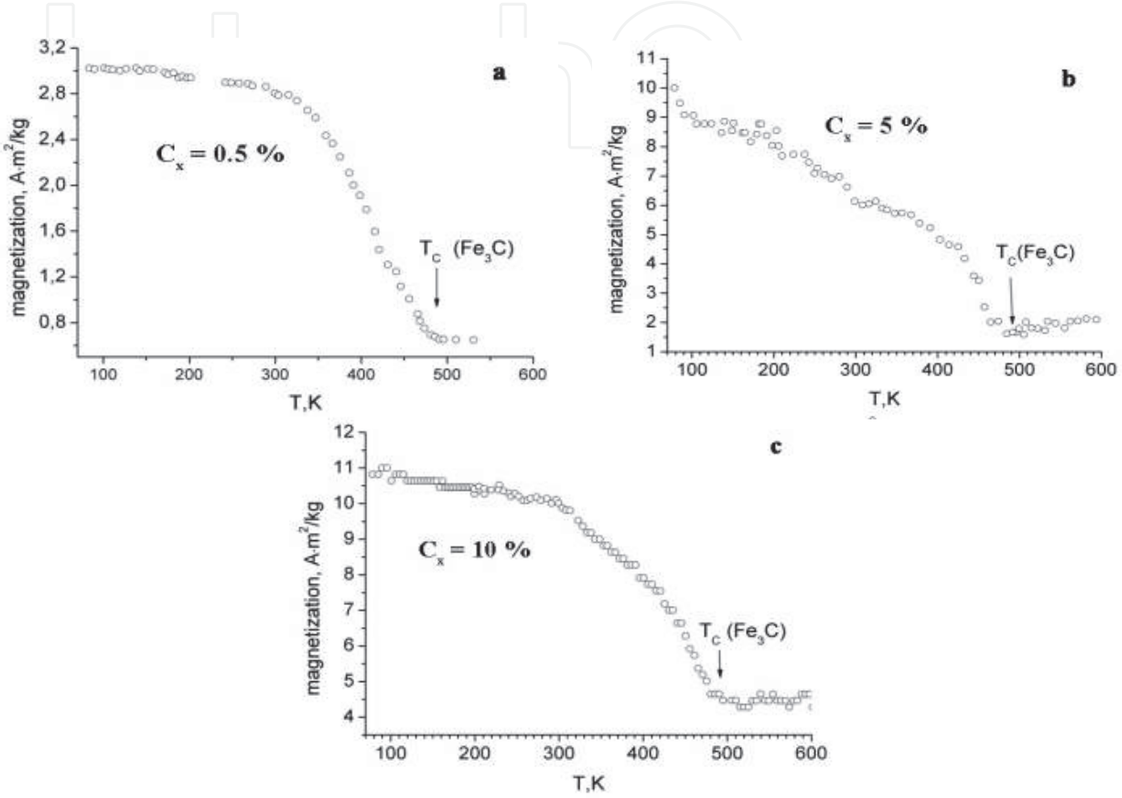

Fig. 11. Temperature dependences σ = $f(T)$ in heating for powder CNTs synthesized at various concentrations of ferrocene c_x in the feeding solution: (a) 0.5%, (b) 5%, and (c) 10%

The facts that the saturation magnetization of 10%-sample is approximately three times the magnetization of 5 % - sample and the coercive force is smaller can be explained by the higher concentration of magnetic inclusions in that sample. This also might be one of the reasons H_c (c_x=10 %) < H_c (c_x=5 %) at low temperatures. One can assume that in the sample with c_x=5% the particles with smaller dimensions prevail, and for them M_s is lower and H_c is higher than in 10 %-sample.

In a general case, the coercive force is proportional to anisotropy and in inverse proportion to specific magnetization. For composites its value can be calculated using the effective anisotropy constant $H_C = 2K_{eff} / M_S$. For MFCNTs K_{eff} value can be estimated by the shape anisotropy (Vas'kovskiya et al., 2007). This implies, taking into consideration the experimental data, that in 5%-samples the decrease of anisotropy occurs faster as the temperature increases in comparison with the decrease of magnetization. In that case it means that the concentration of the nanoparticles of spherical or ellipsoidal shapes dominates. For these particles the temperature fluctuations lead to spontaneous

magnetization more effectively in comparison with, for example, the particles of elongated shape. As a consequence, the effective anisotropy decreases as temperature increases. On the contrary, in 10 %-samples where the coercive force does not decrease with increasing the temperature the particles of elongated shape predominate (or their increased concentration exists). For elongated particles the energy of anisotropy is considerable, and the temperature fluctuations have not significant influence on spontaneous magnetization.

Thus, in case of c_x= 10 % we have conservation of the shape anisotropy with increasing the temperature to 300 K, what can be related to an increase of the concentration of elongated particles. For that type of particles the increase of thermal fluctuations with increasing the temperature does not result in the loss of the shape anisotropy value, as in case of spherical ones or similar ellipsoids. In addition, the origination of bridges between the particles causing the generation of the domain boundaries, as well as particle sticking which closes magnetic fluxes, may influence the effective coercive force.

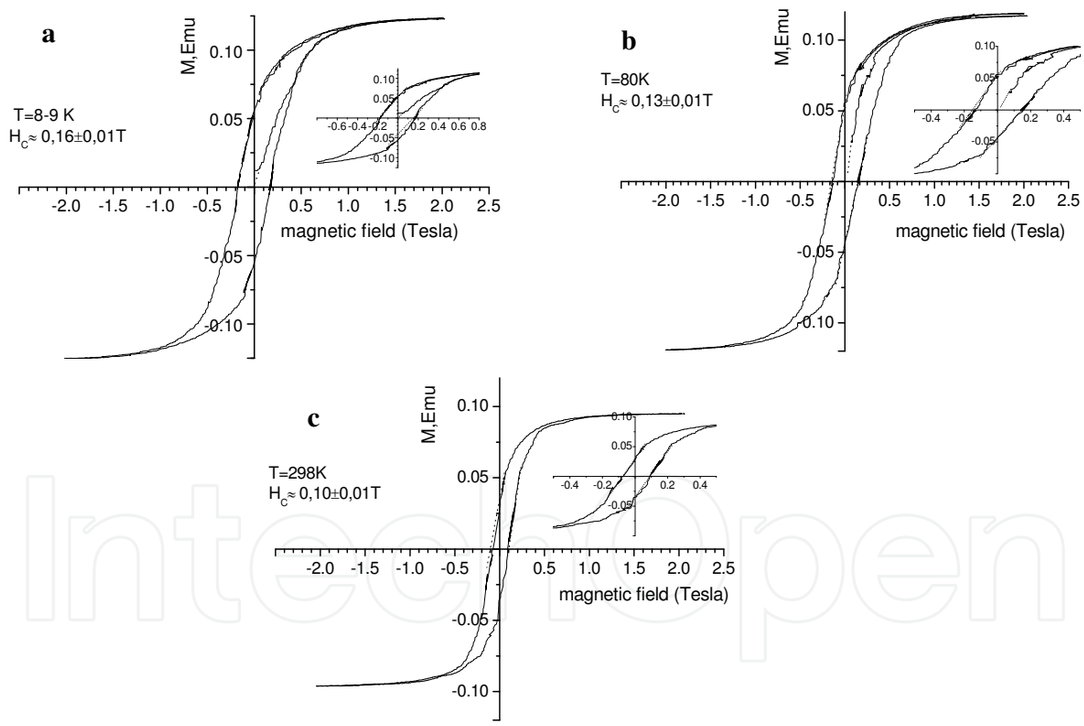

Fig. 12. The hysteresis loops of the non-oriented blocks of MFCNT arrays obtained at 5 % of ferrocene in the feeding solution taken at temperatures: (a) T = 8 K, (b) T = 80 K, (c) T=298.

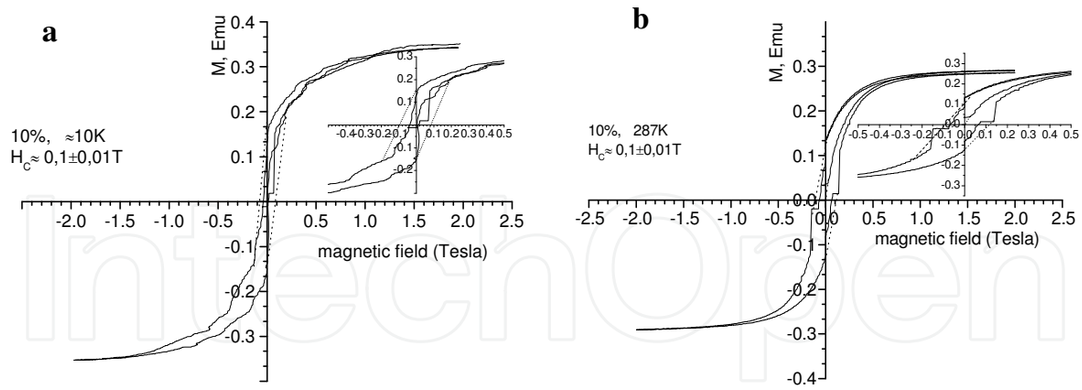

Fig. 13. The hysteresis loops of the non oriented blocks of MFCNT arrays obtained at 10 % of ferrocene in the feeding solution taken at temperatures: (a) T = 10 K, (b) T = 287 K.

5. Model of magnetic structure in Fe_3C nanoparticles

Magnetic structure of individual nanoparticles of various magnetic materials is the subject of numerous theoretical and experimental investigations (Chernavskij, 2002; Cowburn, 1999, 2002; Hollinger et al, 2003; Guslienko & Novosad, 2004; Kondorsky, 1952, 1979; Kravchuk et al., 2007; Kravchuk & Sheka, 2007; Ross et al., 2002; Usov & Peschanyj, 1994).

Nanodisk may reveal either homogeneous or vortex state dependently on its size (radii R and thickness L) as well as on the direction of magnetic field. Magnetization in direction perpendicular to the cross-section of nanodisk means homogeneous perpendicular z-state. In the case when magnetization is parallel to the cross-section of nanodisk – this is in-plane state. When size of nanodisk exceeds correspondent exchange length R_0, configuration of magnetic field tends to overcome the formation of poles on the surface. It resulted in magnetic moments torsion and formation of vortex structure.

In accordance with (Hollinger et al., 2003) the magnetic vortex state of the disk has a fourfold topological degeneracy, since in principle one can measure (and flip) independently both the vorticity of the state and the central polarization (+/-) of the vortex; i.e. one has 2 bit per dot for a 'vortex-state disk', instead of only 1 bit for 'single-domain disk'.

In our theoretical model homogeneous magnetic state of nanodisk is described in continuous approximation applying de-magnetization coefficients.

Vortex structure is characterized with exchange energy normalized per $\pi R^2 L M_S^2$ value (Kravchuk, 2007; Guslienko & Novosad, 2004):

$$w_{ex} = (R / R_0)^2 \int_0^1 d\rho\rho \left[\left(\frac{d\theta}{d\rho} \right)^2 + \frac{\sin^2 \theta}{\rho^2} \right], \tag{4}$$

and magnetostatic energy:

$$w_m = \frac{4\pi}{\beta} \int_0^\infty \left(\int_0^1 \cos\theta(\rho) J_0(\rho x) d\rho \right)^2 [1 - \exp(-\beta x)] dx \,, \tag{5}$$

where $\beta = L / R$, $J_0(z)$ – zero-order Bessel function of the first kind, ρ – polar radius in-plane of the disk, θ(ρ) – angle, characterizing magnetization, M_S – saturation magnetization of nanodisk material.

Euler equation, that minimize total magnetic energy of nanodisk $w_v = w_{ex} + w_m$, possess integral-differentiate form (Guslienko & Novosad, 2004):

$$\frac{d^2\theta(\rho)}{d\rho^2} + \frac{1}{\rho}\frac{d\theta(\rho)}{d\rho} - \frac{\cos\theta(\rho)\sin\theta(\rho)}{\rho^2} = \left(\frac{R}{R_0}\right)^2 \sin\theta(\rho)\int_0^1 \rho'\cos\theta(\rho')g(\rho,\rho',\beta)d\rho', \quad (6)$$

where magnetostatic kernel equals:

$$g(\rho,\rho',\beta) = -\frac{4\pi}{\beta}\int_0^\infty [1-\exp(-\beta x)]J_0(\rho x)J_0(\rho' x)dx \quad (7)$$

It is the authors opinion (Guslienko & Novosad, 2004; Kravchuk et al., 2007; Kravchuk & Sheka, 2007) that equation (6), that could be solved with function $\theta(\rho)$, should be analyzed only approximately. Our analysis shows that elimination of improper kernel integral (7) is possible by application of integral transformations. The first kernel term (4) is transformed using integral Bessel - Hankel transform (Ditkin & Prudnikov, 1961). It will draw to the relationship:

$$g_1(\rho,\rho') = -\frac{4\pi}{\beta}\int_0^\infty J_0(\rho x)J_0(\rho' x)dx = -\frac{4\pi}{\beta}\frac{1}{(\rho+\rho')\Gamma(1)}F\left(\frac{1}{2};\frac{1}{2};1;\frac{4\rho\rho'}{(\rho+\rho')^2}\right), \quad (8)$$

where Γ - gamma-function; F – hypergeometric function of ½, ½, 1 parameters and argument $v = 4\rho\rho'(\rho+\rho')^{-2}$. Applying integral Laplace transform (Ditkin & Prudnikov, 1961) to the second term in (7), we receive the relationship:

$$g_2(\rho,\rho',\beta) = -\frac{4\pi}{\beta}\int_0^\infty \exp(-\beta t)J_0(\rho t)J_0(\rho' t)dt = -\frac{4\pi}{\beta}\left(\frac{1}{\pi\sqrt{\rho\rho'}}Q_{-\frac{1}{2}}\left(\frac{\beta^2+\rho^2+\rho'^2}{2\rho\rho'}\right)\right), \quad (9)$$

where $Q_{-1/2}(x)$ - Legandre spherical function of the second kind of the parameter -½, that is defined using hypergeometric function (Ditkin & Prudnikov, 1961; Gradshtein & Ryzhik, 1971). In so doing,

$$g_2(\rho,\rho',\beta) = -\frac{4\pi}{\beta}\frac{1}{\sqrt{\beta^2+\rho^2+\rho'^2}}F\left(\frac{3}{4};\frac{1}{4};1;\left(\frac{2\rho\rho'}{\beta^2+\rho^2+\rho'^2}\right)^2\right) \quad (10)$$

Obtained relationships (11), (13) allow exact calculation of the function (10). The advantage of applied hypergeometric functions is the absence of improper integrals as well as simplicity and universality of calculations.

Next, equation (6) is transformed to equation containing linear integral term by substitution of desired function $u(\rho) = \cos\theta(\rho)$ and substitution $1-u^2 = 1-4z^2 = f(z)$. Consequently we obtain equation

$$\left(\frac{d^2z}{d\rho^2}\right)-\frac{f_z'(z)}{f(z)}\left(\frac{dz}{d\rho}\right)^2+\frac{1}{\rho}\left(\frac{dz}{d\rho}\right)+\frac{1}{2}f(z)U(\rho)=0\,, \tag{11}$$

where

$$U(\rho)=\left(\frac{u}{\rho^2}+(R/R_0)^2\int_0^1 u(\rho')\rho' g(\beta,\rho,\rho')d\rho'\right), \tag{12}$$

with boundary conditions: $z(0)=1/2$, $dz/d\rho_{\rho=0}=0$.
The solution of non-linear equation (11), in accordance with (Kamkr, 1971), corresponds to the solution of first term $(dz/d\rho)=f(z)\omega(\rho)$, where function $\omega(\rho)$ is defined with linear first term equation $(d\omega/d\rho)+(\omega/\rho)+(1/2)U(\rho)=0$. After integration we obtain the relationship:

$$u(\rho)=\frac{C_1\rho^{4C_2}Y(\rho)-1}{C_1\rho^{4C_2}Y(\rho)+1}\,, \tag{13}$$

where $Y(\rho)=\exp\left(-2\ln\rho\int\rho U(\rho)d\rho+2\int\rho\ln(\rho)U(\rho)d\rho\right)$, C_1, C_2 - constants.

Deduced system of equations (12), (13) for calculation of vortex magnetization distribution in nanodisk contains linear Fredholm equation of the second kind (12) and the expression, combining functions $u(\rho)$ and $U(\rho)$.
Basing on the obtained system of equations (10)-(12) calculations of vortex magnetization distribution in Fe_3C nanodisks 5 to 100 nm in size has been performed. Calculation results were compared with the results, obtained for permalloy using OOMMF software for micromagnetic modeling (The object oriented micromagnetic framework. http://math.nist.gov/oommf/). It has been shown that vortex magnetization distribution is well approximated with the function

$$u_f(\rho)=\frac{C_1-C_2\rho^2-C_3\rho^3}{C_1+C_4\rho^2+C_5\rho^3}\,, \tag{14}$$

where $C_{(1\text{-}5)}$ – constant values, depending on nanodisk's size.
It is established, basing on performed calculations that Gaussian distribution commonly applied as probe function for approximation of magnetization vortex, draw to the significant error and could be used only for description of kernel vortex. Simultaneously, $uf(\rho)$ function practically satisfies the equation (6) in the whole range of radii R and nanodisk thicknesses L. Calculated distributions of vortex magnetization for different radii and thicknesses in Fe_3C nanodisks are presented in Fig. 14. It is shown that an increase of L draw to the increase of the radii of vortex kernel in accordance with the relationship $L^{1/p}$ (p=3.6-4.0), while an increase of R resulted in the proportional decrease of the kernel vortex radii. The size of vortex changed similarly.
Calculated diagram of basic magnetic states in cylindrical Fe_3C nanoparticles for the radii-height plane evidences that exchange length for Fe_3C nanoparticles ranges within 6-8 nm, see Fig. 15. The important conclusion is that within applied approximation vortex state of Fe_3C nanodisks with one central vortex is stable for radii values of 8-16 nm and thickness of 12-80 nm. These results together with well-established thermal stability make Fe_3C

nanoparticles very prospective for application in modern recording media with recording density about 1 Tbit/inch^2.

Proposed model was also applied for consideration of temperature dependencies of the crossover between vortex and homogeneous z-state in the temperature range 300-470 K. It is shown in Fig. 16 that temperature increase supports the crossover from the vortex to homogeneous z-state. At constant values of nanoparticles radii and height temperature growth draw to the increased radii and vortex size. Such peculiar dependencies originate from growing exchange length with temperature.

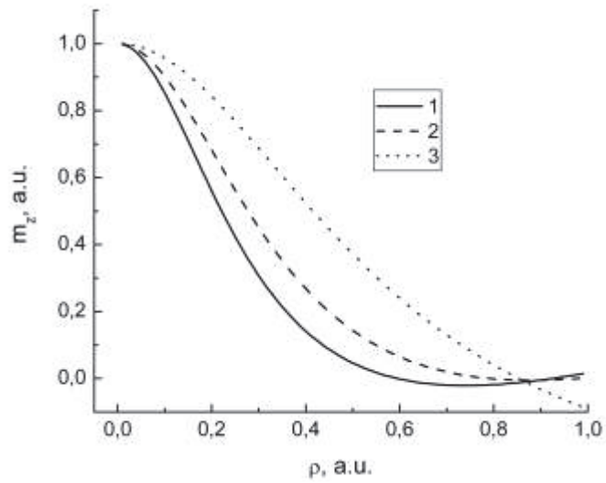

Fig. 14. Distribution of vortex magnetization in Fe_3C nanodisks at β =3.0: $r=R/R_0$=2.5 (curve 1); r=2.0 (2); r=1.2 (3).

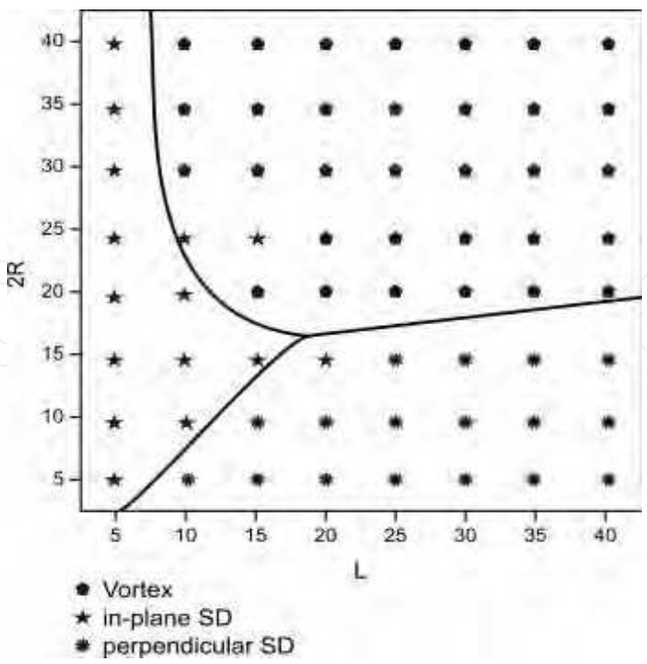

Fig. 15. Diagram of crossovers between different magnetic states for nanodisks (SD) of Fe_3C (analytic and micromagnetic simulation, nm)

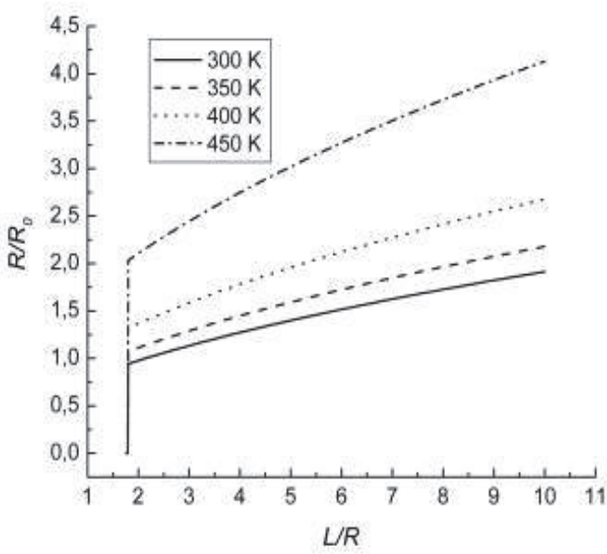

Fig. 16. Temperature dependencies of the radius *R* which defines the crossover between the vortex and the homogeneous perpendicular *z*-state for Fe_3C.

6. Local ^{57}Fe states in carbon nanotubes synthesized by injection CVD method

6.1 Effect of ferrocene concentration c_x

In the present experiment local ^{57}Fe states in MFCNTs were studied by application of Mössbauer spectroscopy as a function of the ferrocene concentration c_x (1 %, 5 % and 10 %) in samples sintered at temperature in the reaction zone T equaled 875°C. The process duration time t was 1 min. The cooling rate of the synthesized MFCNT arrays was determined by the natural cooling down rate of the heating furnace. The injection rate of the feeding solution into the reaction zone v=1 ml·min^{-1} and Ar flow rate v_{Ar}=100 cm^3 ·min^{-1} were provided in all the experiments considered below.

Recorded RT Mössbauer spectra are presented in fig. 17 (a-c), correspondingly. The best fitting of the spectra was performed in assumption of four different subspectra, i.e. singlet *C*, quadrupole doublet *D* and two magnetic sextets S_1 and S_2. Hyperfine parameters of the subspectra are summarized in table 1.

The parameters of singlet C and sextet S_2 are characteristic of fcc γ-Fe and bcc α-Fe, correspondingly. Spectra fitting confirmed (see table 1) that γ-Fe phase, existing at 860 °C in accordance with Fe-C phase diagram, was detected also during the cooling process at all c_x and partially transformed into ferromagnetic α-Fe, Fe_3C and antiferromagnetic FeC_2 phases. It is to admit that the contribution of γ-Fe nanoparticles was quite significant (between 20 % and 31 %). It means that by "quenching" process draw to the formation of thermodynamically stable at ambient conditions γ-Fe phase. The relative contribution of γ-Fe and α-Fe phases for 5% and 10% samples is almost the same, but for 1% is comparably higher. Sextet S_1, should be assigned to the cementite phase Fe_3C in strong correlation with X-ray diffraction data (Basaev et al., 2008). It is important to note the presence of nonmagnetic FeC_2 phase characterized with quadrupole doublet D. The relationship between Fe_3C and FeC_2 phase's contributions revealed the dependency on c_x, in the samples.

In fact, Fe_3C contribution increased with c_x, at the expense of FeC_2. Particularly, at the applied conditions of synthesis Fe_3C content is growing up from 21 % at c_x=1 % up to its higher value 54 % at c_x=10 %.

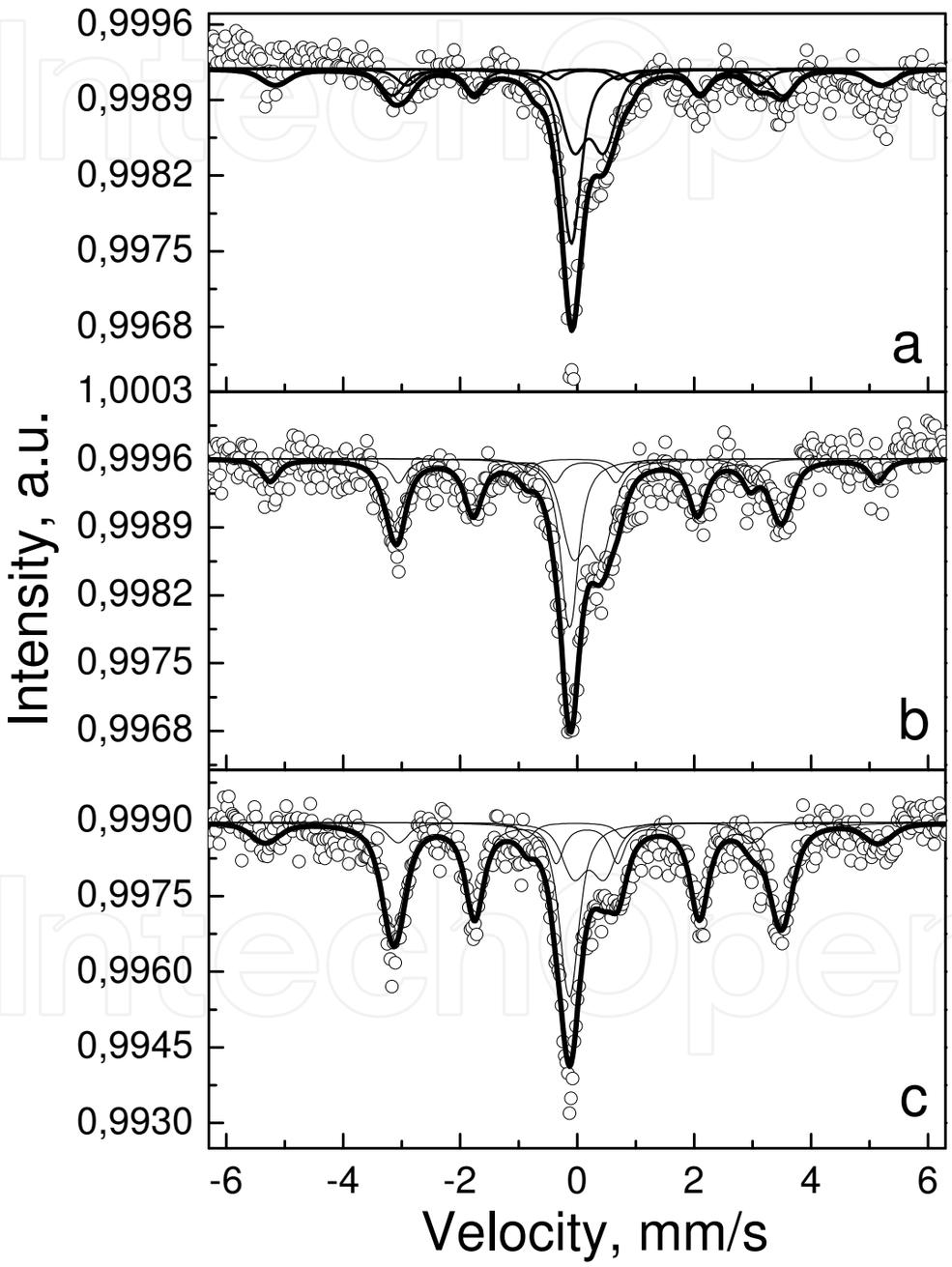

Fig. 17. Mössbauer spectra of MFCNTs synthesized at c_x=1 % (a), c_x =5 % (b) and c_x =10 % (d) (t=1 min, T= 875 ºC, natural cooling down rate of the reactor).

c_x , %	Subspectrum	δ, mm·s^{-1}	ΔE, mm·s^{-1}	H_{eff}, T	Contribution	Phase
1	Singlet C	-0,10	0	-	31	γ-Fe
	Doublet D	0,2	0,52	-	31	FeC_2
	Sextet S_1	0,17	0	20,7	21	Fe_3C
	Sextet S_2	0,06	-0,03	32,2	17	α-Fe
5	Singlet C	-0,13	-0,11	-	21	γ-Fe
	Doublet D	0,17	0,48	-	28	FeC_2
	Sextet S_1	0,16	0,02	20,5	37	Fe_3C
	Sextet S_2	-0,05	0	32,3	14	α-Fe
10	Singlet C	-0,13	0	-	20	γ-Fe
	Doublet D	0,20	0,52	-	13	FeC_2
	Sextet S_1	0,17	0	20,6	54	Fe_3C
	Sextet S_2	-0,06	-0,03	32,6	13	α-Fe

Table 1. Hyperfine parameters of the spectra of MFCNTs synthesized with different concentrations c_x of the feeding solution; δ – isomer shift, ΔE – quadrupole spitting, H_{eff} – hyperfine magnetic field (T=875ºC, t=1 min, slow cooling rate)

6.2 Effect of cooling rate

In the second experiment Mössbauer spectroscopy was applied to investigate influence of cooling rate during MFCNTs synthesis c_x=10 %, T=825 °C, t=4 min. The cooling methods for this case were different: either slow realized by natural cooling down rate, or fast, using Ar stream of 450 cm^3·min^{-1} and immediate extracting of the CNT samples out of the reactor.

Actually, absence of noticeable changes in phase composition was also detected by Mössbauer investigation (fig. 18). Hyperfine parameters extracted by fitting of Mössbauer spectra are presented in the table 2. According to the table 2, as in a case of table 1, Mössbauer spectra could be fitted with four subspectra characterizing γ-Fe, α-Fe, Fe_3C and FeC_2 phases. For the both samples the contribution of cementite is the largest, ~ 82%, and their hyperfine parameters coincide within the error. There is a little difference in contributions of α-Fe subspectra. In the slow-cooled sample 8 % of α-Fe was formed whereas in the fast-cooled one - 6 %. Besides, the width of spectral line of the last sample is larger than that of the first one, evidencing that slow cooling gives better crystallization of α-Fe. Apart from the described above magnetic subspectra two nonmagnetic components – singlet corresponding to γ-Fe and doublet belonging to FeC_2 – were detected. The doublets possess similar hyperfine parameters and almost the same relative contributions in the both samples. The γ-Fe contribution was a little bit higher in the fast-cooled sample (see table 2).

As compared to our results presented in table 1, where the concentration of the feeding solution was the same (c_x=10%), the contribution of Fe-containing phases was different: Fe_3C ~80 % instead of ~50 % (see table 1). In our previous paper [28] the content of cementite phase was even higher (~ 90%). The specific feature of these experiments is the duration of CNT synthesis process: 1 min (for samples described in table 1); 4 min (for samples described in table 2), and 5 min for samples considered in (Basaev et al., 2008). Therefore, the duration of the synthesis process strongly influences the contribution of iron-containing phases, i.e. the higher is the duration, the higher the content of Fe_3C phase will be. It is evident that for the obtaining the maximum amount of Fe_3C phase the process duration of 5 min. is optimal in our experiments. According to (Wei et al., 2006), in the case when the process duration exceeds 20 min., the annealing of Fe is going on, that can lead to the

decomposition of even thermodynamically stable Fe_3C. CNTs destruction and its morphology deterioration take place. External and internal diameters of CNTs and distance between them are enlarging up to 50 %, branching is appearing and number of spherical shape Fe particles is increasing.

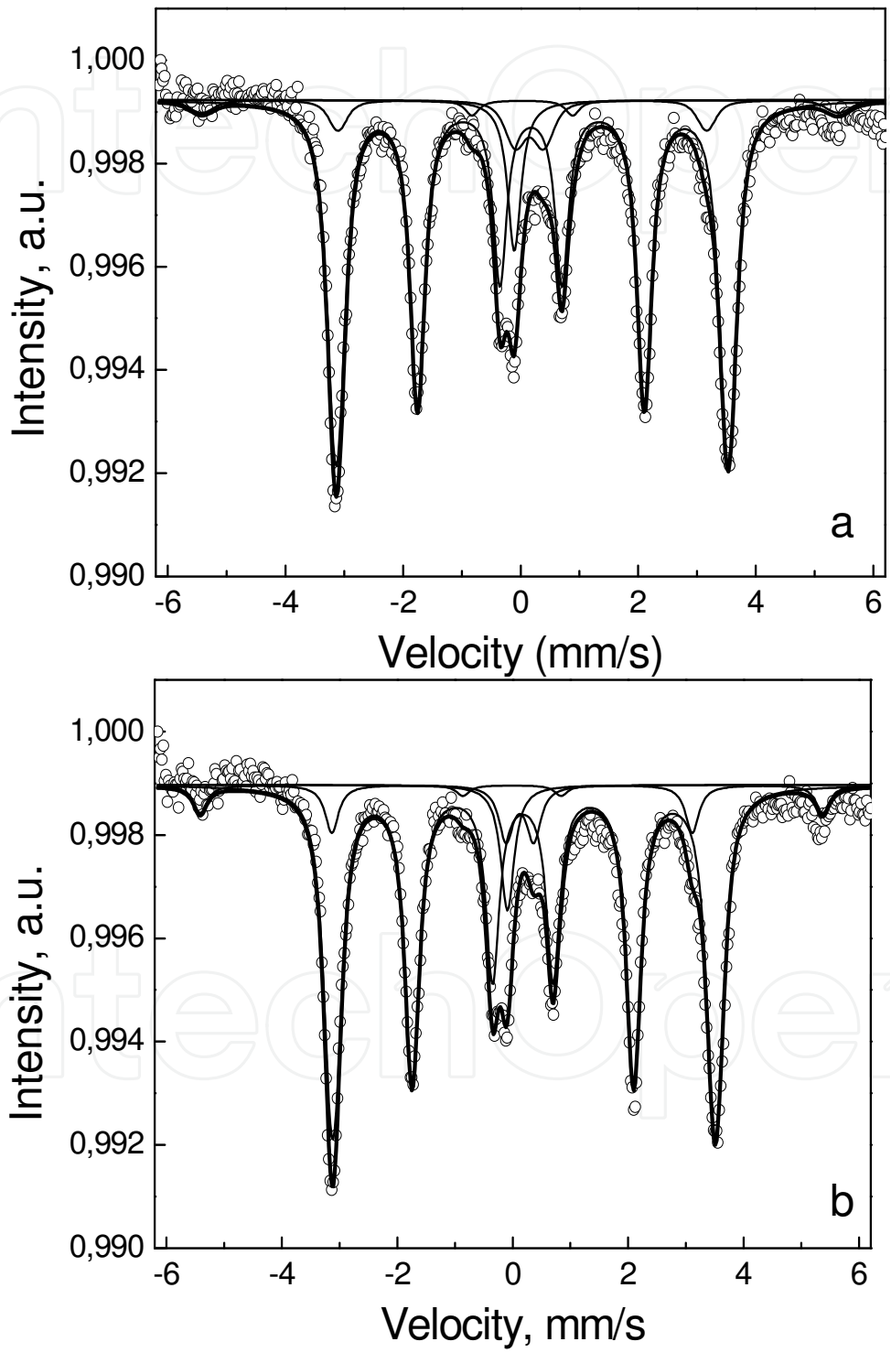

Fig. 18. Mössbauer spectra of MFCNTs synthesized at c_x=10 % t=3.5 min, T= 825 ^{o}C after fast (a) and slow (b) cooling down rates of the synthesis equipment

Cooling	Subspectrum	δ, mm·s^{-1}	ΔE, mm·s^{-1}	H_{eff}, T	Contribution	Phase
fast	Singlet C	-0,11	0	-	7	γ-Fe
	Doublet D	0,15	0,48	-	5	FeC_2
	Sextet S_1	0,18	-0,02	20,7	82	Fe_3C
	Sextet S_2	0,01	0,01	33,6	6	α-Fe
slow	Singlet C	-0,09	0	-	6	γ-Fe
	Doublet D	0,12	0,48	-	5	FeC_2
	Sextet S_1	0,19	0,01	20,6	81	Fe_3C
	Sextet S_2	-0,02	-0,01	33,5	8	α-Fe

Table 2. Hyperfine parameters of the spectra of MFCNTs after fast and slow cooling down rates; δ – isomer shift, ΔE – quadrupole spitting, H_{eff} – hyperfine magnetic field (c_x=10 %, T=825 °C, t=4 min)

6.3 Effect of synthesis temperature

The Mössbauer spectra of the MFCNTs synthesized at two different temperatures, 775 °C and 875 °C, using c_x=1 %; t=4 min and at fast cooling of the furnace after their synthesis are shown in fig. 19.

It is noteworthy that TEM investigations (not shown) did not reveal any new peculiarities in a way the magnetic particles fill nanotubes. Mössbauer spectra of these samples revealed very different phase contributions of Fe-containing phases for two applied synthesized temperatures. As evidenced from the Table 3 summarizing the hyperfine parameters of the corresponding spectra at T=775°C γ-Fe phase was not detected, that is in agreement with the phase diagram of Fe-C. The content of Fe_3C at this temperature is ~60 %, even higher than at c_x=10 % with t=1min (table 1). One should note that at T=775 °C there is very low content of α-Fe phase (only 4 %), and contribution of Fe carbides definitely dominates. It means that at this relatively low temperature the process of γ-Fe phase transformation into other Fe-containing phases was not detected and α-Fe, Fe_3C and FeC_2 phases are directly created during the synthesis process. Large amount of carbides testifies their stability as compared to α-Fe.

Temperature during synthesis, °C	Subspectrum	δ, mm·s^{-1}	ΔE, mm·s^{-1}	H_{eff}, T	Contribution	Phase
875	Singlet C	-0,10	0	-	31	γ-Fe
	Doublet D	0,2	0,52	-	31	FeC_2
	Sextet S_1	0,17	0	20,7	21	Fe_3C
	Sextet S_2	0,06	-0,03	32,2	17	α-Fe
775	Doublet D	0,17	0,50	-	36	FeC_2
	Sextet S_1	0,18	0,02	20,8	60	Fe_3C
	Sextet S_2	0,09	0,15	33,9	4	α-Fe

Table 3. Hyperfine parameters of the spectra of MFCNTs synthesized at 775 °C and 875 °C; δ – isomeric shift, ΔE – quadrupole spitting, H_{eff} – hyperfine magnetic field (c_x =0,5%, t=4min, fast cooling)

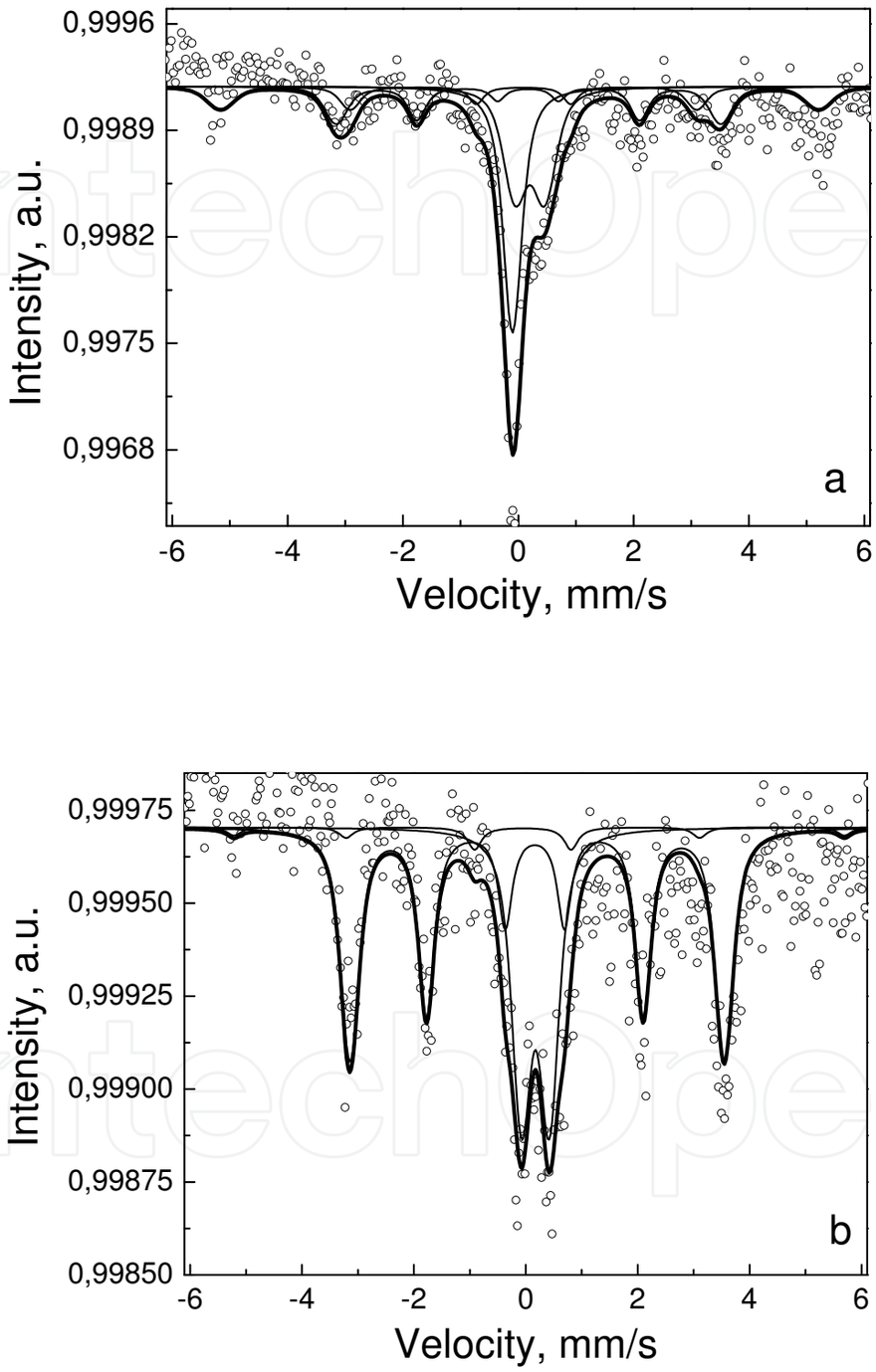

Fig. 19. Mössbauer spectra of the MFCNTs synthesized at two different temperatures, 875°C and 775°C (c_x=1%, t=4 min, fast cooling down rate of the furnace)

7. The influence of electron irradiation on the magnetic properties of carbon nanotubes filled with Fe-phases composite

It is well established that application of CNTs filled with ferromagnetic material as sensors for magnetic scanning probe microscopy, for spintronics devices, high-density magnetic memory materials, biomedicine etc. revealed important requirements to their stability during interaction with electron beams. Lots of theoretical and experimental studies have been conducted on the interaction of electrons with the carbon atoms of the shells of pristine CNTs leading to changes of mechanical, electronic and, correspondingly, electrical properties (Banhart, 1999; Vijayaraghavan et al., 2005; Zhang & Iijima, 2000). However, not many results address the influence of electron irradiation on CNTs filled with the magnetic component. With this respect, we studied the electron irradiation effect on the structure, composition and magnetic properties of CNTs filled with Fe_3C mostly (amount of α-Fe, Fe_5C_2 is negligible).

CNT arrays have been synthesized by the high temperature pyrolysis of the xylene/ferrocene (feeding) solution at atmospheric pressure. Ar was used as a gas-career. The concrete regime of CNT arrays synthesis was chosen as following: the ferrocene concentration c_x in the feeding solution was 0.5%, 5% and 10%, its injection rate into the reaction zone was 1 ml min^{-1}, temperature in the reaction zone was 870°C, and the argon flow rate was 100 cm^3 min^{-1}. The process duration time was 5 minutes. The cooling rate of the synthesized CNTs was determined by the natural cooling down rate of the heating furnace. At these conditions the dense vertically aligned CNT arrays filled with the magnetic Fe-contained nanocomposite were formed at the walls of tubular type quartz reactor. As it was shown previously, the filler inside CNTs represents ~90% of Fe_3C and ~10% of α-Fe and Fe_5C_2 (Basaev et al., 2008). CNTs were mechanically removed from the reactor walls for the exposure to electron irradiation and further investigations.

CNTs were irradiated at room temperature with a dose of 10^{15} cm^{-2} using an electron accelerator.

Typical structures of CNTs synthesized using 10%-feeding solution (i.e. c_x=10%) before and after the electron irradiation are presented in figure 20. TEM investigations showed that the structure of CNT shells in general looks unchanged after the electron irradiation. However, those CNTs filled with the magnetic nanocomposite appear to have absolutely different morphology from it was before (figure 20 a,b). The cylinder-shaped filler nanowires located in CNT channels under e-irradiation were transformed into the ball-shaped particles (figure 20 b). The structure of CNT itself was visibly modified also in this area, i.e. the channel inside CNT almost disappeared, the CNT shell became defective. Such transformations might be caused by a pressure buildup within a nanotube in the process of irradiation which leads to tube collapsing and, correspondingly, filler nanowire squeezing and its final break up (Sun et al., 2006). The observed splitting of the filler particles must certainly influence the magnetic properties of CNTs.

The $\sigma(T)$ dependences were obtained in the temperature range 78 K ≤ T < 600 K in the magnetic field H = 0.86 T in the cooling and heating modes. The $\sigma(T)$ dependences measured upon heating of the CNTs samples with different concentration of ferrocene in the feeding solution before and after electron irradiation are shown in figure 21 (a-c). The anomalous point in the dependence $\sigma(T)$ corresponds to the Curie point T_C ~ 480 K for cementite Fe_3C (Basaev, 2008).

One can observe the decrease of the specific magnetization of the irradiated CNTs both at liquid-nitrogen temperature and in the whole temperature range, what is most probably governed by the structural point defects occurred during the electron irradiation. In figure 22 the dependences $\sigma(T)$ of the irradiated CNTs measured both in the heating and cooling modes in a temperature range $700 \div 800\ \text{K} \le T < 100 \div 300\ \text{K}$ are shown. It is seen that $\sigma(T)$ curve measured upon cooling lies well above another measured upon heating. It means that as the samples were heated during the first circle of $\sigma(T)$ measurements the radiation defects were annealed what resulted in the increase of the specific magnetization which aimed to reach the primary measured values of non-radiated samples. These measurements confirm the fact that the decrease of magnetization of CNTs is governed by the point structural defects created during electron irradiation.

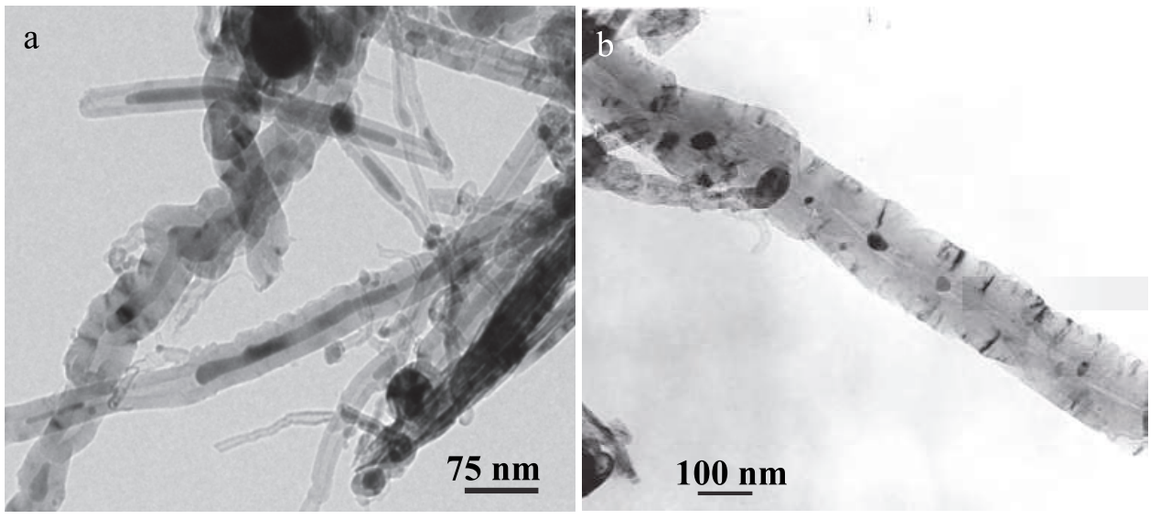

Fig. 20. Typical TEM views of CNTs synthesized using 10%-feeding solution: (a) before and (b) after the electron irradiation.

The comparison of the ratio "signal-background" in the X-ray spectra taken on the CNT specimens synthesized at c_x=10% before and after the e-irradiation with the dose of 10^{15} cm^{-2} (figure 23) revealed the decrease of integral intensity of X-ray reflexes in the angle range $20° < 2\theta < 30°$ corresponding to crystalline state of the carbon composing CNTs. This can be explained by the generation of point defects in the crystal structure caused by Coulomb interaction of incident electrons with the atom nuclei and electron shells of target material. Point defects, such as Frenkel pairs, in contrast to dislocations, do not result in enormous changes of the phase state of material, but just unit cell deformations (Shalayev, 1967). In the angle range $40° < 2\theta < 55°$ which characterizes the Fe_3C and α-Fe the intensity decrease is less pronounced. The integral intensity of the reflexes at large angles in the range $74° < 2\theta < 85°$ before and after the irradiation remains almost the same what is in agreement with (Lipson & Steeple, 1972) since the large angle reflexes are not sensitive to small structure deformations in polycrystals. There wasn't found any new reflexes after the exposure to electron irradiation, so we can fearlessly conclude that the used doses resulted only in crystal structure distortion of the C-Fe_3C-α-Fe-Fe_5C_2 composite.

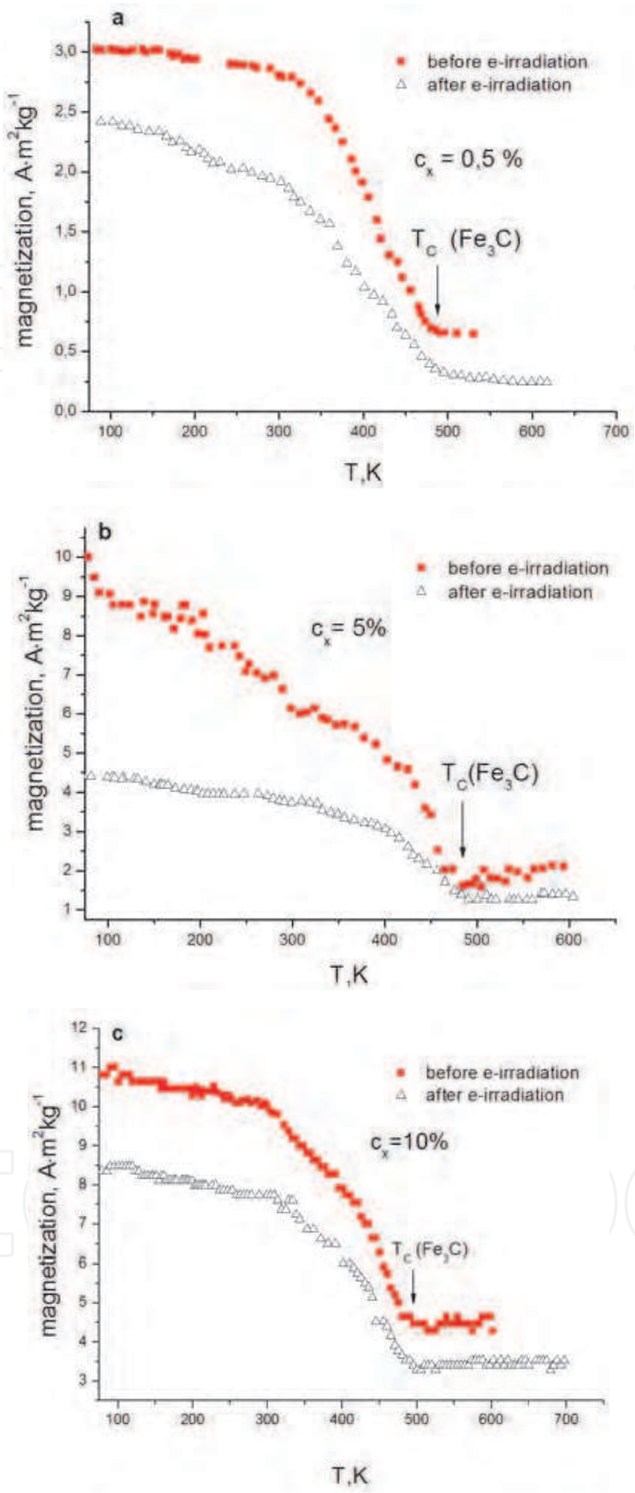

Fig. 21. Temperature dependences $\sigma=f(T)$ of CNTs synthesized using various concentrations of ferrocene in the feeding solution c_x before and after the electron irradiation measured in the heating mode: (a) c_x=0.5%, (b) c_x=5%, (c) c_x=10%.

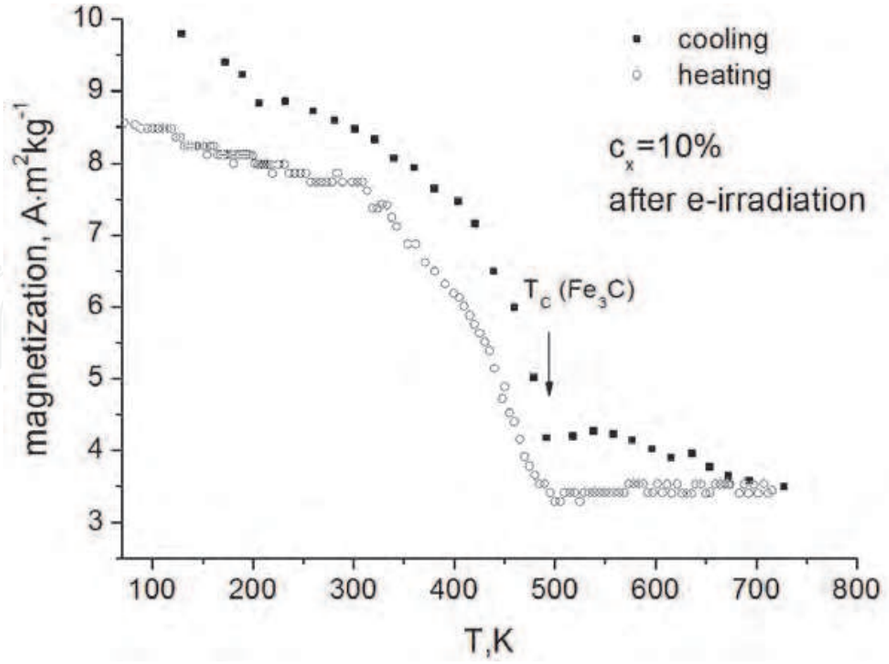

Fig. 22. Temperature dependences $\sigma=f(T)$ of the irradiated CNTs measured in the heating and cooling modes.

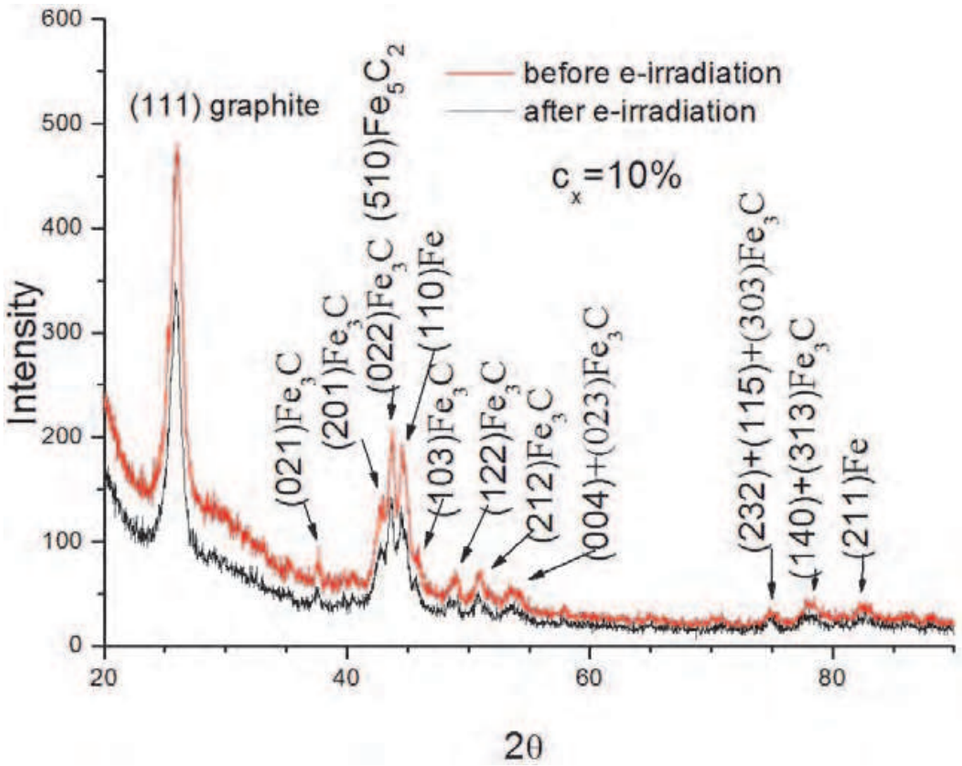

Fig. 23. X-ray diffraction patterns of powder-like nanotube arrays synthesized at 10% of ferrocene in the feeding solution before and after e-irradiation.

8. Acknowledgements

Financial support from State Program for Scientific Research "Functional materials, nanomaterials", project 2.4.12 is gratefully acknowledged.

9. Conclusions

Magnetically functionalized multiwall carbon nanotubes (MFCNT) were synthesized by the high-temperature pyrolysis of liquid hydrocarbon p-xylene C_8H_{10} in a mixture with a volatile catalyst, namely, ferrocene $Fe(C_5H_5)_2$, on the surface of silicon substrates in a quartz reactor. Under the synthesis conditions used in the experiment, arrays of vertically aligned nanotubes are formed on the silicon substrates and reactor walls.

Using different experimental methods it is established that carbon nanotubes of both types exhibit identical properties and represent a complex nanocomposite, C–Fe_3C–Fe_5C_2–Fe. The analysis of the results of X-ray diffraction results, measurements of the specific magnetization, and Mössbauer spectroscopy demonstrated that the Fe_3C content in the filler of the carbon nanotubes is approximately 90%. The unit cell parameters for the structure of the Fe_3C phase in the nanotubes were determined to be a = 0.452 nm, b = 0.508 nm, and c = 0.672 nm. An analysis of the temperature dependences of the specific magnetization $\sigma = f(T)$ demonstrates that, in the temperature range 78 K ≤ T ≤ 1060 K, the magnetic properties of the nanotubes under investigation are governed by the properties of iron carbides (in the form of Fe_3C and Fe_5C_2) and iron. It is revealed that synthesized carbon nanotubes possess reversible magnetic properties in the temperature range 78 K ≤ T ≤ 720 K. The effective magnetic fields on ^{57}Fe nuclei in the composition of the filler components were determined. It was revealed that a certain number of filler particles in the carbon nanotubes possess superparamagnetic properties.

The influence of the catalyst concentration (1%, 5%, and 10%) in the feeding solution on the magnetic properties of the CNT arrays was investigated. X-ray diffraction analysis revealed that the higher the catalyst concentration in feeding solution is, the higher is the content of Fe_3C and Fe phases in the CNTs filler. An analysis of the temperature dependences of the specific magnetization $\sigma=f(T)$ showed that the specific magnetization increases as the ferrocene concentration increases. The temperature dependencies of the specific magnetization demonstrated its higher values for 10%-specimens both lower and higher Curie point of Fe_3C. The anisotropy of the specific magnetization measured perpendicular ($\sigma_\perp$) or parallel ($\sigma_{//}$) to the surface of CNT array inheres in our samples. It was found that $\sigma_\perp > \sigma_{//}$ and both values are higher for the sample prepared at higher concentrations of ferrocene.

The phase composition of magnetic filler located inside of multi-wall MFCNTs was determined be using Mössbauer Spectroscopy. MFCNTs were obtained by the injection CVD method using ferrocene-xylene solution at various conditions (i.e. the ferrocene concentration c_x (0.5%, 5%, and 10%) in the feeding solution, slow or fast cooling down rates of the synthesis reactor, temperature of the reaction zone during synthesis), which may influence the magnetic properties of MFCNTs owing to different contribution of Fe phases. SEM and TEM methods were used to investigate the morphology and structure of the synthesized material. It was shown that Fe_3C phase formation is favorable at relatively low temperatures (775 ^oC) during CNT synthesis, long duration of the CNT growth process, as well as at high content of the catalyst in the feeding solution.

Model of the magnetic structure of cylindrical nanoparticles of cementite Fe_3C was developed. Systems of equations for calculation of the vortex magnetization of the nanoparticles were obtained within continuum approach based on Euler equation minimizing total energy of the cylinder. The temperature effect on single domain size, equal to 6-8 nm at 300 K is also considered. It was shown, that as temperature increases from 300 to 450 K, the single domain size for cementite increases in 2.16 times, and to 470 K – in 3.4 times. The magnetic structure of the cylindrical cementite nanoparticles encapsulated into the carbon nanotubes has been studied in the absence of magnetic field depending on its size in the temperature range of 300-470 K using continuous approximation. The distribution of the magnetization in the cementite nanocylinders has been calculated considering the uniaxial crystallographic anisotropy. The vortex magnetization has been simulated using the rational fractional functions which ensure the required accuracy of the calculations and allow determining the vortex size correctly. It has been shown that the geometrical parameters of the nanoparticles and the temperature are the main factors influencing the transitions between the vortex and homogeneous states. The temperature dependence of the transition between the vortex state and the homogeneous z-state in the temperature range of 300-470 K has been calculated. It has been revealed that the rise in the temperature leads to the vortex size enlarging and promotes the transition from the vortex to either homogeneous or planar states, depending on the size of nanocylinder. The reverse transfers are banned, since the single-domain length increases as the temperature rises.

10. References

Basaev, A.S., Bokhonov, B.B., Demidenko, O.F., Labunov, V.A., Makovetskii, G.I., Prudnikova, E.L., Reznev, A.A., Saurov, A.N., Fedosyuk, V.M., Fedotova, Yu.A., Shulitskii, B.G. & Yanushkevich, K.I. (2008). Synthesis and Properties of Magnetically Functionalized Carbon Nanotubes, *Nanotechnologies in Russia*, Vol. 3, pp. 184–190

Banhart, F. (1999). Irradiation effects in carbon nanostructures, *Rep. Prog. Phys.*, Vol. 62, pp. 1181-1221.

Chechernikov, V. I. (1969). *Magnetic Measurements*, Moscow State University, Moscow (in Russian)

Chikazumi, S. (1980). *Physics of Ferromagnetism, Magnetic Properties of Materials*, Syokabo, Tokyo

Chernavskij, P.A. (2002). New in magnetic methods of investigations of metal-deposited catalysts, *Russian Chemical Journal*, Vol. XLVI, No 3, pp. 19-30 (in Russian)

Cowburn, R.P., Koltsov, D.K., Adeyeye, A.O. & Welland, M.E. (1999). Single-Domain Circular Nanomagnets, *Physical Review Letters*, Vol. 83, No.5, pp. 1042-1045

Cowburn, R.P. (2002). Magnetic nanodots for device applications, *J. Magnetism and Magnetic Materials*, Vol 242-245, Part 1, pp. 505-511

Ditkin, V.A., Prudnikov, A.P. (1961). *Integral transformations and operational calculus*, Fizmatgiz, Moscow (in Russian)

Gradshtein, I.S, Ryzhik, I.M. (1971). *Tables of integrals, sums, series and multiplications*, Nauka, Moscow

Guslienko, K.Yu., Novosad, V. (2004).Vortex state stability in soft magnetic cylindrical nanodots, *J. Applied Physics*, Vol. 96, No. 8, pp. 4451-4455

Harris, P. J. F. (2002). *Carbon Nanotubes and Related Structures*, Cambridge University Press, Cambridge

Hollinger, R., Killinger, A. & Krey, U. (2003). Statics and fast dynamics of nanomagnets with vortex structure, *J. Magnetism and Magnetic Materials*, Vol. 261, pp. 178-189

Joint Committee on Powder Diffraction Standards—International Centre for Diffraction Data (JCPDS—ICDD), PCPDFWIN, Version 2.00, 1998

Kamke, R. (1971). Manual on ordinary differential equations, Nauka, Moscow

Komogortsev, S. V., Iskhakov, R. S., Balaev, A. D., Kudashov, A. G., Okotrub, A. V. & Smirnov, S. I. (2007). Magnetic properties of Fe_3C ferromagnetic nanoparticles encapsulated in carbon nanotubes, *Physics of the Solid State*, Vol. 49, pp. 734-738

Kondorsky, E.I. (1952). To the theory of single-domain particles, *Reports of Academy of Sciences USSR*, Vol. 82, No 3, pp. 365-367 (in Russian)

Kondorsky, E.I. (1979). On the stability of certain magnetic modes in fine ferromagnetic particles, *IEEE Transactions on Magnetics*, Vol. 15, No.5, pp. 1209-1214

Kravchuk, V.P., Sheka, D.D. & Gaididei, Yu.B. (2007). Equilibrium magnetization structures in ferromagnetic nanorings, *J. Magnetism and Magnetic Materials*, Vol. 310, pp.116-125

Kravchuk, V.P., Sheka, D.D. (2007). Thin ferromagnetic nanodisk in out-of-plane magnetic field, *Solid State Physics*, Vol. 49, No 10, pp. 1834-1841 (in Russian)

Labunov, V. A., Shulitski, V. G. (2005). Nonrestricted Large Area of Vertically Aligned Carbon Nanotubes, *Proceedings of the III Russian–Japanese Seminar "Advanced Technological Processes, Materials, and Equipment for Production of Solid-State Electronics Elements and Nanomaterials MISiS–ULVAC"*, Moscow, Russia, April 11–12, 2005

Labunov, V. A., Shulitski, B. G. & Prudnikava, E. L. (2006). High-Efficiency Method of Selective CNT Arrays growth on the Metal/Dielectric/Semiconductor Substrates for FEDs Application, *Digest of Technical Papers of the International Symposium, Seminar and Exhibition (SID-2006)*, San Francisco, United States, June 4–9, 2006.

Li, De-Ch., Dai, L., Huang, Sh., Mau, A. W.H. & Wang, Zh. L. (2000). Structure and growth of aligned carbon nanotube films by pyrolysis. *Chem. Phys. Lett.*, Vol. 316, pp. 349-355

Lipson, H., Steeple, H. (1970). *Interpretation of X-ray Powder Diffraction Patterns*, Macmillan, London

Lipson, G., Steeple, H. (1972). *Interpretation of powder X-ray spectra*, Mir, Moscow (in Russian)

Pul, Ch. (2005). *Nanotechnologies*, Technosfera, Moscow (in Russian)

Ross, C.A., Hwang, M. & Shima, M. et al. (2002). Micromagnetic behavior of electrodeposited cylinder arrays, *Physical Review B*, Vol. 65, pp. 144417(1)-(8)

Shalayev, A.M. (1967). *Interaction of ionizing radiation with metals and alloys*, Atomizdat, Moscow (in Russian)

Sun, L., Banhart, F., Krasheninnikov, A., Rodriguez-Manzo, J.A., Terrones, M. & Ajayan, P. (2006). Carbon nanotubes as high-pressure cylinders and nano-extruders, *Science*, Vol. 312, pp. 1199-1205

Usov, N.A., Peschanyj, S.E. (1994). Vortex distribution of magnetization in thin ferromagnetic cylinder, *The Physics of Metals and Metallography*, Vol. 78, pp. 13-24 (in Russian)

Varnakov, S.N., Bartolomé, J., Sesé, J. Ovchinnikov, S.G., Komogortsev, S.V., Parshin A.S. & Bondarenko, G.V. (2007). Size effects and magnetization of (Fe/Si) n multilayer film nanostructures, *Physics of the Solid State*, Vol. 49, pp. 1470-1475

Vas'kovskiya, V.O., Patrin, G. S., Velikanov, D. A., Svalov, A. V., Savin, P. A., Yuvchenko, A. A. & Shchegoleva, N. N. (2007). Magnetism of Co layers in a Co/Si multilayer film, *Physics of the Solid State*, Vol. 49, pp.302-307

Vijayaraghavan, A., Kanzaki, K., Suzuki, S., Kobayashi, Y., Inokawa, H., Ono, Y., Kar, S. & Ajayan, P.M. (2005). Metal-semiconductor transition in single-walled carbon nanotubes induced by low-energy electron irradiation, *Nano Lett.*, Vol.5, pp. 1575-1578.

Wei, B., Shima, M., Pati, R., Nayak, S. K., Singh, D.J., Ma, R., Li, Y., Bando, Y., Nasu, S. & Ajayan, P. M. (2006). Room-Temperature Ferromagnetism in Doped Face-Centered Cubic Fe Nanoparticles, *Small*, Vol.2, pp. 804–809

Zhang, Y., Iijima, S. (2000). Microstructural evolution of single-walled carbon nanotubes under electron irradiation, *Philos. Mag. Lett.*, Vol.80, pp. 427-433

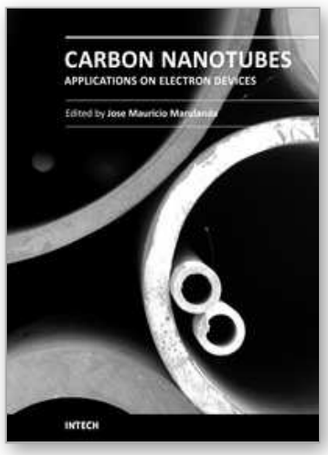

Carbon Nanotubes Applications on Electron Devices

Edited by Prof. Jose Mauricio Marulanda

ISBN 978-953-307-496-2
Hard cover, 556 pages
Publisher InTech
Published online 01, August, 2011
Published in print edition August, 2011

Carbon nanotubes (CNTs), discovered in 1991, have been a subject of intensive research for a wide range of applications. In the past decades, although carbon nanotubes have undergone massive research, considering the success of silicon, it has, nonetheless, been difficult to appreciate the potential influence of carbon nanotubes in current technology. The main objective of this book is therefore to give a wide variety of possible applications of carbon nanotubes in many industries related to electron device technology. This should allow the user to better appreciate the potential of these innovating nanometer sized materials. Readers of this book should have a good background on electron devices and semiconductor device physics as this book presents excellent results on possible device applications of carbon nanotubes. This book begins with an analysis on fabrication techniques, followed by a study on current models, and it presents a significant amount of work on different devices and applications available to current technology.

How to reference

In order to correctly reference this scholarly work, feel free to copy and paste the following:

Vladimir Labunov, Alena Prudnikava, Kazimir Yanushkevich, Aleksander Basaev, Alexander Danilyuk, Yulia Fedotova and Boris Shulitskii (2011). Synthesis and Properties of the Arrays of Magnetically Functionalized Carbon Nanotubes, Carbon Nanotubes Applications on Electron Devices, Prof. Jose Mauricio Marulanda (Ed.), ISBN: 978-953-307-496-2, InTech, Available from: http://www.intechopen.com/books/carbon-nanotubes-applications-on-electron-devices/synthesis-and-properties-of-the-arrays-of-magnetically-functionalized-carbon-nanotubes

INTECH
open science | open minds

InTech Europe
University Campus STeP Ri
Slavka Krautzeka 83/A
51000 Rijeka, Croatia
Phone: +385 (51) 770 447
Fax: +385 (51) 686 166
www.intechopen.com

InTech China
Unit 405, Office Block, Hotel Equatorial Shanghai
No.65, Yan An Road (West), Shanghai, 200040, China
中国上海市延安西路65号上海国际贵都大饭店办公楼405单元
Phone: +86-21-62489820
Fax: +86-21-62489821

IntechOpen